

Distinguishing Kerr naked singularities and black holes using the spin precession of a test gyro in strong gravitational fields

Chandrachur Chakraborty^{1,*}, Prashant Kocherlakota^{1,†}, Mandar Patil^{2,‡},

Sudip Bhattacharyya^{1,§}, Pankaj S. Joshi^{1,¶} and Andrzej Królak^{2,**}

¹*Tata Institute of Fundamental Research, Mumbai 400005, India and*

²*Institute of Mathematics of Polish Academy of Sciences, Śniadeckich 8, 00-956 Warsaw, Poland*

We study here the precession of the spin of a test gyroscope attached to a stationary observer in the Kerr spacetime, specifically, to distinguish naked singularity (NS) from black hole (BH). It was shown recently that for gyros attached to static observers, their precession frequency became arbitrarily large in the limit of approach to the ergosurface. For gyros attached to stationary observers that move with non-zero angular velocity Ω , this divergence at the ergosurface can be avoided. Specifically, for such gyros, the precession frequencies diverge on the event horizon of a BH, but are finite and regular for NS everywhere except at the singularity itself. Therefore a genuine detection of the event horizon becomes possible in this case. We also show that for a near-extremal NS ($1 < a_* < 1.1$), characteristic features appear in the radial profiles of the precession frequency, using which we can further distinguish a near-extremal NS from a BH, or even from NS with larger angular momentum. We then investigate the Lense-Thirring (LT) precession or nodal plane precession frequency of the accretion disk around a BH and NS to show that clear distinctions exist for these configurations in terms of radial variation features. The LT precession in equatorial circular orbits increases with approach to a BH, whereas for NS it increases, attains a peak and then decreases. Interestingly, for $a_* = 1.089$, it decreases until it vanishes at a certain radius, and acquires negative values for $a_* > 1.089$ for a certain range of r . For $1 < a_* < 1.089$, a peak appears, but the LT frequency remains positive definite. There are important differences in accretion disk LT frequencies for BH and NS and since LT frequencies are intimately related to observed QPOs, these features might allow us to determine whether a given rotating compact astrophysical object is BH or NS.

* chandrachur.chakraborty@tifr.res.in

† k.prashant@tifr.res.in

‡ mpatil@impan.pl

§ sudip@tifr.res.in

¶ psj@tifr.res.in

** krolak@impan.pl

I. INTRODUCTION

An important issue in relativistic astrophysics and gravitation theory today has been to rule out the existence of naked singularities in the gravitational collapse of massive matter clouds. Alternatively, if NSs do exist as endstates of massive stars collapsing under self-gravity towards the end of their life-cycles, the important physical question would then be, how can one decide whether a particular astrophysical compact object is a BH or NS. This is a key issue, really at the heart of making physical predictions about very strong gravity regions in the universe, which major astrophysical missions are probing currently [1].

In this connection, it is important to examine in some detail the Kerr geometry configurations, and find physical quantities that can be used to differentiate the BH from NS. The Kerr spacetime describes either a rotating BH or NS, depending on the Kerr spin parameter a , which is the specific angular momentum (J/M). The Kerr BH possesses two event horizons and two ergoregions which are the outer and inner event horizons and outer and inner ergoregions. The region between the outer event horizon and outer ergoradius is called the outer ergoregion or simply the ergoregion. Here, we will be primarily concerned with this region. Similarly, the region between the inner event horizon and the inner ergoradius is called the inner ergoregion. The inner ergoregion is often dismissed as being unphysical since we do not really know reliably what happens behind the outer event horizon of a rotating black hole. The rotational energy of the BH can be extracted by a particle from the outer ergoregion (henceforth, just ergoregion) and this is called the Penrose process.

The ergoregion is responsible for several interesting phenomena, of which one has been recently discussed in Ref.[2] where the exact Lense-Thirring (LT) precession frequency of a test gyroscope in Kerr spacetime has been derived and it was shown that the LT precession frequency diverges on the boundary of the ergoregion (henceforth, ‘ergosurface’) of a BH. For BHs, the dimensionless Kerr parameter satisfies $a_* = J/M^2 \leq 1$. In another work [3], the spin precession frequency was discussed in detail in the case of NS ($a_* > 1$). For NS, the entire region between the inner and outer ergo radii is defined to be the ergoregion. It has been discussed there that the drastic change in geometry of the ergoregion for $a_* > 1$, as opposed to $a_* \leq 1$, could allow for a differentiation of the two space-times using a physical quantity, namely the precession frequency of gyroscopes attached to static observers placed around these compact objects. Specifically, for the NS configuration, along the pole a finite angle opens up where the ergoregion is absent and $r = 0$ can be accessible via this region without passing through the ergoregion. This region broadens on increasing the value of a_* beyond 1 and the ergoregion shrinks toward the equator. It was discussed that the precession frequency always diverges on the ergosurface. Since the ergoregion completely bounds a BH, on ‘approaching’ it in any direction, one would find a divergence. Whereas, in the case of NS, the frequency remains finite and regular in the ‘opening angle’ due to the absence of the ergoregion. We find this to be a possible experiment to distinguish the two qualitatively distinct Kerr configurations.

It was discussed in Ref.[4] how a non-rotating black hole can be distinguished from a naked singularity. In this paper, we discuss how one can distinguish a rotating BH from NS using the behavior of the precession frequency of the spin of a test gyro which moves, in general, along a non-geodesic orbit around such a Kerr compact object, thus generalizing the earlier work on distinguishing black holes from naked singularities. In this regard, we find it useful to mention that recently Bini et al. have analyzed the precession of a test gyroscope along bound [5] and unbound [6] equatorial plane geodesic orbits around a BH with respect to a static reference frame whose axes point towards ‘fixed stars.’ It is well known that the paths followed by spinning test particles are not, in general, geodesics [7, 8].

In the present article, we discuss the precession of a gyroscope both outside and inside the ergoregion of a BH and NS. We find that the divergence of the spin precession frequency on the ergosurface reported in Ref.[3] can be avoided if the test gyro moves with a non-zero angular velocity Ω . In Ref.[3], the motivation was to study the precession of spins of gyroscopes attached to stationary observers, that is, to answer physical questions like ‘how the gyroscope of an astronaut holding his spaceship at a constant distance from a Kerr compact object will behave.’ The four-velocity (u) of ‘static gyros’ on the ergosurface satisfies $u.u = 0$, that is, it becomes null. However, if one introduces an azimuthal component to the four-velocity, the norm can be made non-zero and time-like. We can therefore extend the study of the behavior of a gyro into the ergoregion. We find that the precession frequency of the gyro behaves differently inside the ergoregion of a BH versus that of a NS, due to the presence of the event horizon, therefore rendering it a viable physical quantity that can be used to distinguish a BH from NS.

We note that the Killing vectors of the Kerr spacetime provide invariant characterizations of the ergosurfaces and horizons. The time translation Killing vector ∂_0 is the unique Killing vector that approaches a unit timelike vector at spatial infinity and its vanishing norm gives the invariant location of the ergosurface. Further, one can construct a Killing vector from a linear combination, with constant coefficients, of ∂_0 and the azimuthal

Killing vector ∂_ϕ . The vanishing norm of this Killing vector, for some fixed Ω (say $\Omega = \Omega_H$), can be used to invariantly determine the location of the horizon. With this motivation, we consider here the precession of the spin of gyroscopes attached to stationary observers, whose velocity vectors are proportional to the Killing vectors $K = \partial_0 + \Omega\partial_\phi$. These gyroscopes move along circular orbits around the central compact object with a constant angular velocity Ω which at any given (r, θ) can be chosen to be in a particular range, so that K is timelike. Indeed, when the spacetime describes a BH, this frequency becomes arbitrarily large for observers located infinitesimally close to the horizon, in all coordinates. We interpret this as a coordinate invariant method to locate the horizon. For NS, a divergence in the precession frequency occurs at the singularity itself, which is present in the equatorial plane. In [3], the precession frequency of gyroscopes attached to static observers was considered, namely observers that do not change their spatial position with time. The velocity vectors of these observers are proportional to ∂_0 and we found that the precession frequency for static observers located infinitesimally close to the ergosurface became arbitrarily large, in all coordinates, thus invariantly indicating the location of the ergosurface.

In a later section, we examine the Lense-Thirring precession frequency and the fundamental frequencies of an accretion disk around a Kerr compact object as the other distinguishing criterion of a NS from BH. Stable circular orbits in the equatorial plane for both the BH and NS cases are investigated, and we show that there are important characteristic differences which can be used to distinguish the BH and NS configurations from each other. Specifically, we find the features of stable circular orbits in the equatorial plane for both the BH and NS cases. We also show that the radial and epicyclic frequencies show rather distinct features in the BH and NS cases. Further, in observed QPOs from accretion disks, if one finds a clear peak at some radius, then the existence of NSs could possibly be established.

The scheme of the paper is as follows. In Sec.II, we discuss stationary observers. We outline the derivation for the spin precession frequency of a test gyro which rotates with a non-zero angular velocity in a general stationary and axisymmetric spacetime in Sec.III. We use this expression for the precession frequency specifically for the Kerr spacetime and discuss its features in various useful regimes of the spacetime in Sec.IV. Characteristic features of the precession frequency of a gyroscope orbiting NSs and BHs that can be used to distinguish them, in principle, are described in Sec.V. Further, in Sec.VI, features which can be used to distinguish near-extremal NSs from NSs with higher angular momentum are discussed. In Sec.VII, we use the Lense-Thirring precession (orbital plane precession) of an accretion disk around a Kerr spacetime as another distinguishing criterion. We also discuss observational aspects related to QPOs. Finally Sec.VIII outlines our results and conclusions.

II. STATIONARY OBSERVERS IN KERR SPACETIME

In a rotating spacetime, observers can remain still without changing their location with respect to infinity only outside the ergoregion. Such observers are called static observers [9, 10] and their four-velocity is given as

$$u_{\text{static}}^\sigma = u_{\text{static}}^t (1, 0, 0, 0). \quad (1)$$

Once inside the ergoregion, it is impossible to stay fixed to a point without changing all three spatial coordinates (say, r, θ, ϕ) of their world lines with time. The ergoregion is a characteristic feature of non-static stationary spacetimes. Specifically, in the case of the BH, its event horizon lies inside the ergoregion. This means that, in general, static observers cannot exist arbitrarily close to the horizon of black hole. In contrast, an observer can hover very close to the horizon of a Schwarzschild black hole, remaining fixed. However, it is possible for observers to fix (r, θ) and rotate (prograde only) around a BH or NS inside their ergoregion, with respect to infinity. Such observers are called stationary observers and their four-velocity is given as

$$u_{\text{statio}}^\sigma = u_{\text{statio}}^t (1, 0, 0, \Omega) \quad (2)$$

where t is the time coordinate and Ω is the angular velocity of the observer. Since we are interested in studying timelike observers, the values that Ω takes are restricted. This is true outside the ergoregion as well and retrograde rotating observers are then allowed. Let us henceforth call gyroscopes attached to static and stationary observers static gyroscopes and stationary gyroscopes respectively, for brevity.

III. SPIN PRECESSION OF A TEST GYROSCOPE: FORMALISM

Let us consider a test gyroscope attached to a stationary observer, which moves along a Killing trajectory in a stationary spacetime. The spin of such a gyroscope undergoes Fermi-Walker transport along,

$$u = (-K^2)^{-\frac{1}{2}} K, \quad (3)$$

where K is the timelike Killing vector field. In this special situation, it is known that the gyroscope precession frequency coincides with the vorticity field associated with the Killing congruence. That is, this gyroscope rotates relative to a corotating frame with an angular velocity and this effect is generally known as the ‘‘gravitomagnetic precession,’’ since the vorticity vector plays the role of a magnetic field in the 3 + 1 splitting of spacetime [11]. Thus, the general spin precession frequency of a test gyro, Ω_s , is the rescaled vorticity field of the observer congruence and can be expressed as [10]

$$\begin{aligned} \tilde{\Omega}_s &= \frac{1}{2K^2} * (\tilde{K} \wedge d\tilde{K}) \\ \text{or, } (\Omega_s)_\mu &= \frac{1}{2K^2} \eta_\mu^{\lambda\beta\delta} K_\lambda \partial_\beta K_\delta, \end{aligned} \quad (4)$$

where Ω_s is the spin precession frequency in coordinate basis, $*$ represents the Hodge star operator or Hodge dual, $\eta^{\mu\lambda\beta\delta}$ represent the components of the volume-form in spacetime and \tilde{K} , $\tilde{\Omega}_s$ are the one-forms of K and Ω_s respectively. In any stationary spacetime, K can be chosen to be $K = \partial_0$ for which, from Eq.(4), Ω_s becomes Ω_{LT} , the Lense-Thirring (LT) precession frequency. This can be expressed as [2, 10],

$$\Omega_{\text{LT}} = \frac{1}{2} \frac{\varepsilon_{ijl}}{\sqrt{-g}} \left[g_{0i,j} \left(\partial_l - \frac{g_{0l}}{g_{00}} \partial_0 \right) - \frac{g_{0i}}{g_{00}} g_{00,j} \partial_l \right]. \quad (5)$$

In a static spacetime, LT precession vanishes since $g_{0i} = 0$. On the other hand, it does not vanish in a stationary spacetime. Moreover, due to the presence of $K^2 = g_{00}$ in the denominator, Eq.(4) and Eq.(5) diverge if g_{00} vanishes. In a stationary and axisymmetric spacetime, this happens only on the ergosurface, which makes K a null vector there. Inside the ergoregion, K is no longer timelike but becomes spacelike. Thus, Eq.(5) is invalid inside the ergoregion as well as on its boundary.

Since the focal point of this paper is to study spin precession in the Kerr spacetime, we point out here that it has two Killing vectors: the time translation Killing vector ∂_0 and the azimuthal Killing vector ∂_ϕ . Any constant coefficient linear combination $K = \partial_0 + \Omega \partial_\phi$ is also a Killing vector and this exhausts the set of Killing vectors in the Kerr spacetime. As stated earlier, the Killing vector ∂_0 is the unique Killing vector that approaches a unit timelike vector at spatial infinity. We now consider the full timelike Killing vector of the Kerr space-time and study spin precession for observers with u , that is stationary observers. This is in contrast to [3], where the velocity was chosen to be proportional ∂_0 and these described static observers. Therefore, for a general stationary spacetime which also possess a spacelike Killing vector we can write the most general timelike Killing vector as,

$$K = \partial_0 + \Omega \partial_c. \quad (6)$$

where ∂_c is a spacelike Killing vector of that stationary spacetime and Ω , for an observer moving along integral curves of K , represents the angular velocity. The metric of this particular spacetime is independent of x^0 and x^c coordinates. The corresponding co-vector of K is,

$$\tilde{K} = g_{0\nu} dx^\nu + \Omega g_{\gamma c} dx^\gamma, \quad (7)$$

where $\gamma, \nu = 0, c, 2, 3$ in 4-dimensional spacetime. Separating space and time components we can write \tilde{K} as

$$\tilde{K} = (g_{00} dx^0 + g_{0c} dx^c + g_{0i} dx^i) + \Omega (g_{0c} dx^0 + g_{cc} dx^c + g_{ic} dx^i) \quad (8)$$

where $i = 2, 3$. Since we are mainly interested in the ergoregion of a stationary and axisymmetric spacetime, we can abolish g_{0i} and g_{ic} terms. Finally, we obtain

$$\tilde{K} = (g_{00} dx^0 + g_{0c} dx^c) + \Omega (g_{0c} dx^0 + g_{cc} dx^c) \quad (9)$$

and

$$d\tilde{K} = (g_{00,k} dx^k \wedge dx^0 + g_{0c,k} dx^k \wedge dx^c) + \Omega (g_{0c,k} dx^k \wedge dx^0 + g_{cc,k} dx^k \wedge dx^c). \quad (10)$$

Now, Eq.(4) can be modified as

$$\tilde{\Omega}_p = \frac{1}{2K^2} * (\tilde{K} \wedge d\tilde{K}). \quad (11)$$

Substituting the expressions of \tilde{K} and $d\tilde{K}$ in Eq.(11), we obtain the one-form of the precession frequency ¹ as:

$$\begin{aligned} \tilde{\Omega}_p = & \frac{\varepsilon_{ckl} g_{l\mu} dx^\mu}{2\sqrt{-g} \left(1 + 2\Omega \frac{g_{0c}}{g_{00}} + \Omega^2 \frac{g_{cc}}{g_{00}} \right)} \\ & \left[\left(g_{0c,k} - \frac{g_{0c}}{g_{00}} g_{00,k} \right) + \Omega \left(g_{cc,k} - \frac{g_{cc}}{g_{00}} g_{00,k} \right) + \Omega^2 \left(\frac{g_{0c}}{g_{00}} g_{cc,k} - \frac{g_{cc}}{g_{00}} g_{0c,k} \right) \right] \end{aligned} \quad (12)$$

where we have used $*(dx^0 \wedge dx^k \wedge dx^c) = \eta^{0kcl} g_{l\mu} dx^\mu = -\frac{1}{\sqrt{-g}} \varepsilon_{ckl} g_{l\mu} dx^\mu$ and $K^2 = g_{00} + 2\Omega g_{0c} + \Omega^2 g_{cc}$.

Corresponding vector (Ω_p) of the co-vector $\tilde{\Omega}_p$ is

$$\begin{aligned} \Omega_p = & \frac{\varepsilon_{ckl}}{2\sqrt{-g} \left(1 + 2\Omega \frac{g_{0c}}{g_{00}} + \Omega^2 \frac{g_{cc}}{g_{00}} \right)} \\ & \left[\left(g_{0c,k} - \frac{g_{0c}}{g_{00}} g_{00,k} \right) + \Omega \left(g_{cc,k} - \frac{g_{cc}}{g_{00}} g_{00,k} \right) + \Omega^2 \left(\frac{g_{0c}}{g_{00}} g_{cc,k} - \frac{g_{cc}}{g_{00}} g_{0c,k} \right) \right] \partial_l. \end{aligned} \quad (13)$$

In a stationary and axisymmetric spacetime with coordinates $0, r, \theta, \phi$, Eq.(13) reduces to

$$\begin{aligned} \tilde{\Omega}_p = & \frac{1}{2\sqrt{-g} \left(1 + 2\Omega \frac{g_{0\phi}}{g_{00}} + \Omega^2 \frac{g_{\phi\phi}}{g_{00}} \right)} \\ & \left[-\sqrt{g_{rr}} \left[\left(g_{0\phi,\theta} - \frac{g_{0\phi}}{g_{00}} g_{00,\theta} \right) + \Omega \left(g_{\phi\phi,\theta} - \frac{g_{\phi\phi}}{g_{00}} g_{00,\theta} \right) + \Omega^2 \left(\frac{g_{0\phi}}{g_{00}} g_{\phi\phi,\theta} - \frac{g_{\phi\phi}}{g_{00}} g_{0\phi,\theta} \right) \right] \hat{r} \right. \\ & \left. + \sqrt{g_{\theta\theta}} \left[\left(g_{0\phi,r} - \frac{g_{0\phi}}{g_{00}} g_{00,r} \right) + \Omega \left(g_{\phi\phi,r} - \frac{g_{\phi\phi}}{g_{00}} g_{00,r} \right) + \Omega^2 \left(\frac{g_{0\phi}}{g_{00}} g_{\phi\phi,r} - \frac{g_{\phi\phi}}{g_{00}} g_{0\phi,r} \right) \right] \hat{\theta} \right]. \end{aligned} \quad (14)$$

For $\Omega = 0$, Eq.(14) reduces to

$$\tilde{\Omega}_p|_{\Omega=0} = \frac{1}{2\sqrt{-g}} \left[-\sqrt{g_{rr}} \left(g_{0\phi,\theta} - \frac{g_{0\phi}}{g_{00}} g_{00,\theta} \right) \hat{r} + \sqrt{g_{\theta\theta}} \left(g_{0\phi,r} - \frac{g_{0\phi}}{g_{00}} g_{00,r} \right) \hat{\theta} \right], \quad (15)$$

which is only applicable outside the ergoregion. This is the LT precession frequency of a test gyro due to the rotation of any stationary and axisymmetric spacetime [12, 13].

A. Application to Kerr Spacetime

We now apply the above formalism to the Kerr spacetime to describe the behavior of a test gyro both inside and outside ergoregion. The Kerr metric in Boyer-Lindquist coordinates can be written as

$$ds^2 = - \left(1 - \frac{2Mr}{\rho^2} \right) dt^2 - \frac{4Mar \sin^2 \theta}{\rho^2} d\phi dt + \frac{\rho^2}{\Delta} dr^2 + \rho^2 d\theta^2 + \left(r^2 + a^2 + \frac{2Mra^2 \sin^2 \theta}{\rho^2} \right) \sin^2 \theta d\phi^2 \quad (16)$$

where a is the specific angular momentum, defined as $a = J/M$ and,

$$\rho^2 = r^2 + a^2 \cos^2 \theta, \quad \Delta = r^2 - 2Mr + a^2. \quad (17)$$

For convenience, we also define the dimensionless Kerr parameter $a_* = a/M = J/M^2$, which we shall use almost exclusively. The various metric components can be read off from Eq.(16) and we have,

$$\sqrt{-g} = \rho^2 \sin \theta. \quad (18)$$

¹ Ω_p is not the LT precession frequency of the gyro. Since the gyro has a non-zero angular velocity Ω , the precession frequency Ω_p is modified. If we set $\Omega = 0$, we have $\Omega_p = \Omega_{LT}$. In this work, the expression of Ω_p describes the overall precession which includes the LT effect as well as some other effects (for e.g., geodetic precession) which we will discuss as we proceed.

Substituting the metric components of Kerr spacetime into Eq.(14), we obtain the spin precession frequency of a gyroscope to be,

$$\vec{\Omega}_p = \frac{A \sqrt{\Delta} \cos \theta \hat{r} + B \sin \theta \hat{\theta}}{\rho^3 [(\rho^2 - 2Mr) + 4\Omega Mar \sin^2 \theta - \Omega^2 \sin^2 \theta [\rho^2(r^2 + a^2) + 2Ma^2r \sin^2 \theta]]}, \quad (19)$$

where,

$$\begin{aligned} A &= 2aMr - \frac{\Omega}{8} [8r^4 + 8a^2r^2 + 16a^2Mr + 3a^4 + 4a^2(2\Delta - a^2) \cos 2\theta + a^4 \cos 4\theta] + 2\Omega^2 a^3 Mr \sin^4 \theta, \\ B &= aM(r^2 - a^2 \cos^2 \theta) + \Omega [a^4 r \cos^4 \theta + r^2(r^3 - 3Mr^2 - a^2M(1 + \sin^2 \theta)) \\ &\quad + a^2 \cos^2 \theta(2r^3 - Mr^2 + a^2M(1 + \sin^2 \theta))] + \Omega^2 aM \sin^2 \theta [r^2(3r^2 + a^2) + a^2 \cos^2 \theta(r^2 - a^2)]. \end{aligned} \quad (20)$$

B. Range of Ω

Eq.(19) is valid both inside and outside the ergoregion. From the requirement that u be timelike,

$$K^2 = g_{\phi\phi}\Omega^2 + 2g_{t\phi}\Omega + g_{tt} < 0, \quad (21)$$

we can calculate the restricted range of Ω . Therefore, the allowed values of Ω at any fixed (r, θ) are,

$$\Omega_-(r, \theta) < \Omega(r, \theta) < \Omega_+(r, \theta) \quad (22)$$

with,

$$\Omega_{\pm} = \frac{-g_{t\phi} \pm \sqrt{g_{t\phi}^2 - g_{\phi\phi}g_{tt}}}{g_{\phi\phi}}. \quad (23)$$

Specifically, in the Kerr spacetime,

$$\Omega_{\pm} = \frac{2Mar \sin \theta \pm \rho^2 \sqrt{\Delta}}{\sin \theta [\rho^2(r^2 + a^2) + 2Ma^2r \sin^2 \theta]}, \quad (24)$$

which shows that the range of allowed values for Ω becomes increasingly limited as the observer is located close to the horizon, that is $r \sim r_+$, and is eventually limited to the single value at the horizon of the BH,

$$\Omega_H = \frac{a}{2Mr_+}. \quad (25)$$

Further, in the equatorial plane ($\theta = \pi/2$), Eq.(24) becomes

$$\Omega_{\pm}|_{\theta=\pi/2} = \frac{2Ma \pm r\sqrt{\Delta}}{r(r^2 + a^2) + 2Ma^2}. \quad (26)$$

Since the ergoregion for NSs always extends all the way up to the ring singularity in the equatorial plane, we can evaluate $\Omega_{\pm}|_{\theta=\pi/2}$ at $r = 0$ and, from Eq. (26), it is evident that these two frequencies match at the singularity. Therefore, we must point out that both at the horizon (r_+) and at the ring singularity ($r = 0, \theta = \pi/2$), there exist no valid values for Ω (because of the strict inequality) implying that no time-like stationary observer can exist at these points. Our precession frequency expression is not valid at these points but it is still meaningful and illuminating to study and plot its limiting values at these points.

We can see from panel (a) of Fig.1 that $\Omega_+|_{\theta=\pi/2}$ and $\Omega_-|_{\theta=\pi/2}$ match at $r \rightarrow r_+$, for a BH with $a_* = 0.9$, and the value of Ω becomes $\Omega_H \approx 0.31$. Panel (c) of the same figure shows that a small gap appears between the same two quantities at $r \approx M$ in case of the near-extremal NS with $a_* = 1.001$ and the two curves match with one another at $r \rightarrow 0$ with the value of $\Omega = 1/a_*$. In the case of NS with higher angular momentum, say, for $a_* = 2$ (see panel (b)), the small gap disappears at $r = M$ and the two curves match at $r \rightarrow 0$, as usual for NSs.

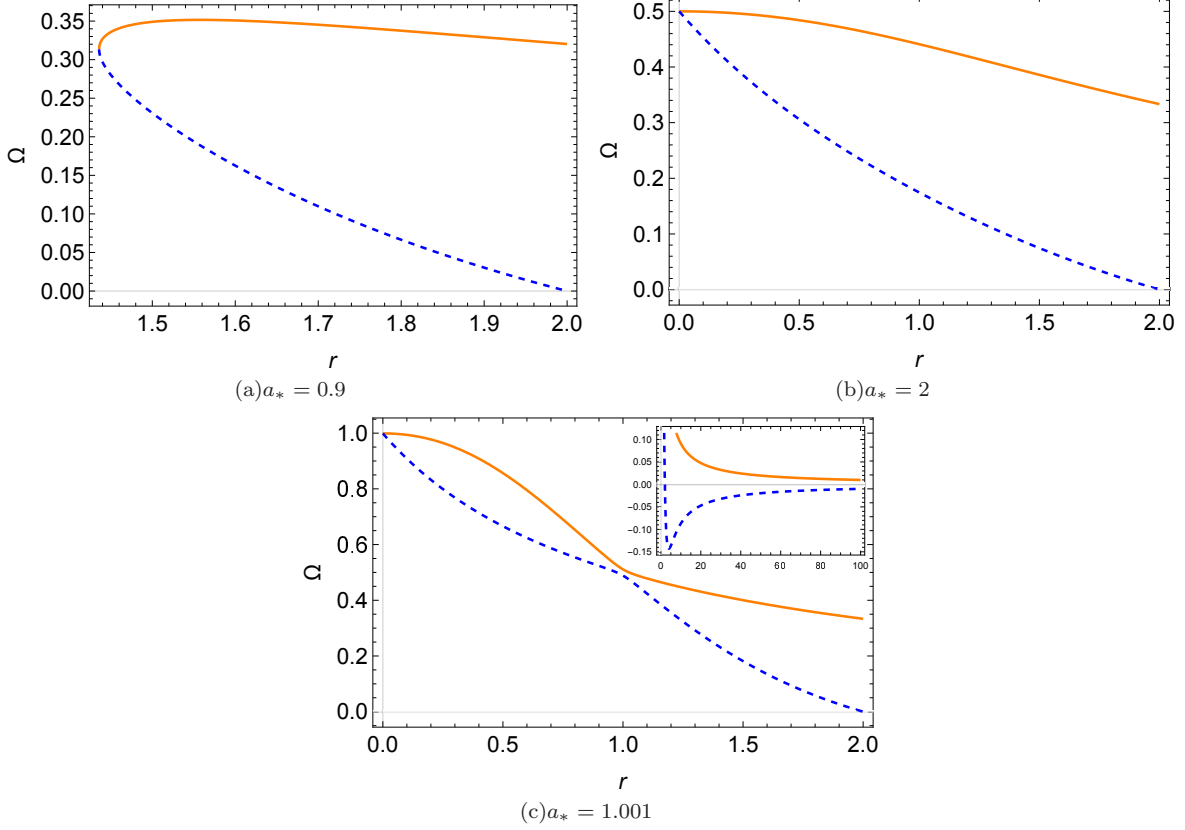


FIG. 1. The frequency of a stationary gyroscope Ω can only take values in the range: (Ω_-, Ω_+) at any (r, θ) . Ω_- and Ω_+ (in M^{-1}) are in dashed blue and orange respectively and have been plotted specifically inside the ergoregion, in the equatorial plane ($\theta = \pi/2$), as a function of r (in M) for different values of Kerr parameter a_* . The inset in panel (c) shows Ω_{\pm} outside the ergoregion, for reference. This is the boundary of the region in which the most general Killing vector in Kerr spacetime, $K = \partial_0 + \Omega\partial_\phi$, is time-like. For black holes, we can see from panel (a) that Ω_{\pm} meet at the horizon. For NSs, we can see from panels (b), (c) that Ω_{\pm} meet at the singularity. Further, it can be seen from (c), that for near-extremal NSs ($a_* \sim 1$), Ω_{\pm} take close values near $r = 1$, which was the location of the horizon of the extremal BH ($a_* = 1$).

To compare the behavior of the gyro inside the ergoregion of a BH and NS, one can now plot $\Omega_p = |\vec{\Omega}_p|$ with r at different θ for observers with varying Ω . For this purpose, we introduce the parameter q to scan the range of allowed values for Ω as follows,

$$\Omega = q \Omega_+ + (1 - q) \Omega_- = \omega - (1 - 2q) \sqrt{\omega^2 - \frac{g_{tt}}{g_{\phi\phi}}} = \frac{2Mar \sin \theta - (1 - 2q) \rho^2 \sqrt{\Delta}}{\sin \theta [\rho^2 (r^2 + a^2) + 2Ma^2 r \sin^2 \theta]} \quad (27)$$

where $0 < q < 1$ and $\omega = -g_{t\phi}/g_{\phi\phi}$. Clearly, the range of q covers the entire range of Ω from Ω_+ to Ω_- . Now, using the expression for Ω , from Eq.(27), we can simplify the denominator of Eq.(19) and obtain a nice and compact expression for the spin precession frequency,

$$\vec{\Omega}_p = \frac{(r^2 + a^2)^2 - a^2 \Delta \sin^2 \theta}{4q(1 - q) \rho^7 \Delta} \left[A \sqrt{\Delta} \cos \theta \hat{r} + B \sin \theta \hat{\theta} \right], \quad (28)$$

where $0 < q < 1$ and A and B have been given in Eq.(20).

If we use the expression for Ω from Eq.(27) in Eq.(6), we obtain

$$K = \frac{qK_+ + (1 - q)K_-}{\|qK_+ + (1 - q)K_-\|} = \frac{qK_+ + (1 - q)K_-}{\sqrt{2q(1 - q)K_+ \cdot K_-}} \quad (29)$$

where K_{\pm} , the two null vectors associated with Ω_{\pm} , are given as (see Eq.6)

$$K_{\pm} = \partial_t + \Omega_{\pm} \partial_{\phi}. \quad (30)$$

Further, in a general stationary and axisymmetric spacetime, we can write $K_+ \cdot K_- = 2(g_{tt} - \omega^2 g_{\phi\phi})$.

C. Acceleration of the test gyroscope

The gyroscopes we consider here have a specific velocity u and, in general, experience non-zero acceleration. They follow helical paths tangent to the Killing trajectory and the acceleration experienced by these gyroscopes is not arbitrary. This acceleration might be provided by using large amounts of rocket power or some other source of thrust and we can calculate the necessary acceleration scalar, for our gyros, using the following expression of the 4-acceleration,

$$\alpha_{\beta} = \frac{1}{2} \nabla_{\beta} \ln |K^2|. \quad (31)$$

We find the acceleration scalar for u to be

$$\begin{aligned} \alpha = \sqrt{g^{\beta\gamma} \alpha_{\beta} \alpha_{\gamma}} = & -\frac{1}{\rho^5 K^2} \left[\Delta \left\{ M(2r^2 - \rho^2) [1 - a\Omega \sin^2 \theta]^2 - r\rho^4 \Omega^2 \sin^2 \theta \right\}^2 \right. \\ & \left. + \sin^2 \theta \cos^2 \theta \left\{ 2Mr [a - \Omega(r^2 + a^2)]^2 + \Omega^2 \rho^4 \Delta \right\}^2 \right]^{\frac{1}{2}}, \end{aligned} \quad (32)$$

where K^2 is

$$K^2 = g_{\phi\phi} \Omega^2 + 2g_{t\phi} \Omega + g_{tt} = \frac{-4q(1-q)\rho^2 \Delta}{(r^2 + a^2)^2 - a^2 \Delta \sin^2 \theta}. \quad (33)$$

Therefore, Eq.(32) reduces to

$$\begin{aligned} \alpha = \frac{(r^2 + a^2)^2 - a^2 \Delta \sin^2 \theta}{4q(1-q)\rho^7 \Delta} \left[\Delta \left\{ M(2r^2 - \rho^2) [1 - a\Omega \sin^2 \theta]^2 - r\rho^4 \Omega^2 \sin^2 \theta \right\}^2 \right. \\ \left. + \sin^2 \theta \cos^2 \theta \left\{ 2Mr [a - \Omega(r^2 + a^2)]^2 + \Omega^2 \rho^4 \Delta \right\}^2 \right]^{\frac{1}{2}}. \end{aligned} \quad (34)$$

Eq.(34) represents the amount of acceleration that is needed to move the test gyro in the Kerr spacetime. It is also evident from the above expression that the acceleration becomes arbitrarily high, blowing up as the event horizon is approached from any direction. Since NSs do not possess horizons, the acceleration of the gyro remains finite all along including at $r = 0$ ($\theta \neq \pi/2$), which we can see from,

$$\alpha|_{r=0} = \frac{1}{4q(1-q)a^2 \cos^3 \theta} [M^2(1 - a\Omega \sin^2 \theta)^4 + a^6 \Omega^4 \sin^2 \theta \cos^2 \theta]^{\frac{1}{2}}. \quad (35)$$

However, the above expression diverges close to the ring singularity ($r = 0, \theta = \pi/2$). The acceleration of the gyro (Eq.32) vanishes if it rotates in a geodesic with the Kepler frequency

$$\Omega = \Omega_{\phi} = \pm \frac{M^{\frac{1}{2}}}{r^{\frac{3}{2}} \pm aM^{\frac{1}{2}}}. \quad (36)$$

D. Zero Angular Momentum Observer

We note that for $q = 0.5$, Ω becomes the characteristic ZAMO frequency ω ,

$$\omega = \frac{2Mar}{(r^2 + a^2)^2 - a^2 \Delta \sin^2 \theta} = -\frac{g_{t\phi}}{g_{\phi\phi}}. \quad (37)$$

In this case, test gyros attached to stationary observers regard both $+\phi$ and $-\phi$ directions equivalently, in terms of the local geometry, and see photons symmetrically [9]. These gyros are non-rotating relative to the local

spacetime geometry. The angular momentum of such a “locally non-rotating” observer is zero and is therefore called a zero angular momentum observer (ZAMO), first introduced by Bardeen [9, 14]. Bardeen et al.[15] showed that the ZAMO frame is a powerful tool in the analysis of physical processes near astrophysical objects. Here, we should note that Eq.(31) reduces to Eq.(33.23) of (see Exercise 33.4) [9] in the case of a ZAMO in a general stationary and axisymmetric spacetime.

IV. USEFUL LIMITS

In this section, we will explore various useful limits of the spin precession frequency (Eq.28). We discuss what happens to the frequency as $r \rightarrow 0$ (specifically, the ring singularity is at $r = 0, \theta = \pi/2$), how it looks like in the equatorial plane $\theta = \pi/2$ and whether this frequency vanishes in the Schwarzschild spacetime.

A. Behavior of $\vec{\Omega}_p$ at $r = 0$.

As discussed earlier, our expression for $\vec{\Omega}_p$ is not valid at the ring singularity ($r = 0, \theta = \pi/2$). However, we can still study its behavior in its vicinity, that is, in the region $r = 0, 0 \leq \theta < 90^\circ$. We note here that this region is strictly completely outside the ergoregion since the ergosurface meets the ring singularity (see Figs.1 and 2 of Ref.[3]). At $r = 0$, Eq.(19) becomes

$$\vec{\Omega}_p|_{r=0} = \frac{-a^2\Omega[3 + 4\cos 2\theta + \cos 4\theta] \hat{r} - 4M \sin 2\theta[1 - a\Omega(1 + \sin^2 \theta) + a^2\Omega^2 \sin^2 \theta] \hat{\theta}}{8a^2 \cos^4 \theta [1 - a^2\Omega^2 \sin^2 \theta]}, \quad (38)$$

where we have used, from Eq.(20),

$$\begin{aligned} A|_{r=0} &= -\frac{a^4\Omega}{8} [3 + 4\cos 2\theta + \cos 4\theta], \\ B|_{r=0} &= -Ma^3 \cos^2 \theta [1 - a\Omega(1 + \sin^2 \theta) + a^2\Omega^2 \sin^2 \theta]. \end{aligned} \quad (39)$$

In the above expressions, the allowed range of Ω is

$$-\frac{1}{a \sin \theta} < \Omega < \frac{1}{a \sin \theta}. \quad (40)$$

Since we are outside the ergoregion, we can consider static observers, that is we set $\Omega = 0$ and Eq.(38) reduces to

$$|\vec{\Omega}_p| = \frac{M}{a^2} \tan \theta \sec^2 \theta, \quad (41)$$

and matches with our earlier calculations of Ref.[3] and can be seen from Eq.(6) and (7) therewith. Therefore, Ω_p varies from $0 \leq \Omega_p < \infty$ for $0 \leq \theta < 90^\circ$ at $r = 0$. That is, it diverges only on the ring singularity (which is at $x^2 + y^2 = a^2, z = 0$ in Cartesian Kerr-Schild coordinates) but is finite *inside* it ($x^2 + y^2 < a^2, z = 0$).

It is useful to mention here that one can smoothly, in principle, go over to the region with ‘negative r ’ (i.e., $r < 0$) in Kerr spacetime, which is tantamount to passing through the ring singularity. but we stop at $r = 0$ and avoid probing negative values of r . The reason behind stopping at $r = 0$ is that it is fairly widely accepted that quantum gravity will resolve the singularity resulting in a compact overspinning object with boundary at a positive value of r , which is referred to as ‘superspinar’ [16]. Thus the region with negative values of r will be excised and pathological features such as closed timelike curves which occur in $r < 0$ region will not arise. Thus we restrict our probe of the Kerr spacetime to $r \geq 0$.

B. Behavior of $\vec{\Omega}_p$ in the equatorial plane, $\theta = \pi/2$

The precession frequency in the equatorial plane is,

$$\vec{\Omega}_p|_{\theta=\pi/2} = \frac{aM + \Omega(r^3 - 3Mr^2 - 2Ma^2) + aM\Omega^2(3r^2 + a^2)}{r^2 [(r - 2M) + 4\Omega Ma - \Omega^2[r(r^2 + a^2) + 2Ma^2]]}, \quad (42)$$

with the range Ω determined from Eq.(26). Specifically, at the ergosurface ($r = 2M$) the precession frequency becomes

$$\vec{\Omega}_p|_{\theta=\pi/2, r=2M} = \frac{a - 2\Omega(a^2 + 2M^2) + a\Omega^2(a^2 + 12M^2)}{16\Omega M^2[a - \Omega(a^2 + 2M^2)]} \quad (43)$$

with Ω being restricted to (see FIG.1 also)

$$0 < \Omega < \frac{a}{a^2 + 2M^2}. \quad (44)$$

That is, if the mass or angular momentum of the central object increases, the allowed range of Ω at the ergosurface, in the equatorial plane, decreases.

For extremal BHs ($a_* = 1$), the precession frequencies at the outer ergoregion and at the outer event horizon respectively can be obtained as

$$\vec{\Omega}_p|_{\theta=\pi/2, r=2M, a_*=1} = \frac{1 - 6\Omega M + 13\Omega^2 M^2}{16\Omega M^2[1 - 3\Omega M]} ; \vec{\Omega}_p|_{\theta=\pi/2, r=M, a_*=1} = -\frac{1}{M}. \quad (45)$$

C. Non-zero $\vec{\Omega}_p$ in the Schwarzschild spacetime

Now, if we set $a = 0$, the Kerr spacetime reduces to the Schwarzschild spacetime, which is *non-rotating*. From Eq.(19), we obtain

$$\vec{\Omega}_p|_{a=0} = \Omega \frac{(r - 3M) \sin \theta \hat{\theta} - (r^2 - 2Mr)^{\frac{1}{2}} \cos \theta \hat{r}}{r - 2M - r^3 \Omega^2 \sin^2 \theta} \quad (46)$$

where Ω can take any value such that u is timelike. Since the Schwarzschild spacetime is spherically symmetric, we can write Eq.(46) for $\theta = \pi/2$ as

$$\Omega_p|_{a=0} = \Omega \frac{r - 3M}{r - 2M - r^3 \Omega^2}. \quad (47)$$

This means that a gyroscope moving in the Schwarzschild spacetime, which is a static spacetime, will precess. Now, if the gyro moves along a circular geodesic Ω should be the Kepler frequency, i.e., $\Omega_{Kep} = (M/r^3)^{1/2}$ and Eq.(47) reduces to

$$\Omega_p|_{a=0, \Omega=\Omega_{Kep}} = \Omega = \left(\frac{M}{r^3}\right)^{\frac{1}{2}}. \quad (48)$$

The above expression gives the precession frequency in the Copernican frame, computed with respect to the proper time τ . The proper time τ , measured in the Copernican frame, is related to the coordinate time t via $d\tau = \sqrt{1 - \frac{3M}{r}} dt$ and we can obtain the precession frequency in the coordinate basis Ω' as,

$$\Omega' = \left(\frac{M}{r^3}\right)^{\frac{1}{2}} \sqrt{1 - \frac{3M}{r}}. \quad (49)$$

We can now find the frequency associated with the change in the angle of the spin vector over, say, one complete revolution around the central object. This is just the difference of Ω' and Ω [17], and we get

$$\Omega_{\text{geodetic}} = \left(\frac{M}{r^3}\right)^{\frac{1}{2}} \left(1 - \sqrt{1 - \frac{3M}{r}}\right), \quad (50)$$

where we have identified above that this precession is just due to geodetic precession (Ω_{geodetic}). This agrees with standard results [18].

V. DISTINGUISHING KERR NAKED SINGULARITIES FROM KERR BLACK HOLES USING THE PRECESSION OF A TEST GYRO

In this section, we point out the characteristic differences in the behavior of the modulus of the spin precession frequency (Ω_p) of stationary gyroscopes for BHs and NSs. We show that the value of Ω_p becomes arbitrarily large for such gyroscopes, located arbitrarily close to the horizon of a BH, that is $r \sim r_+$, for all values of q except $q = 0.5$, the ZAMO frequency. However, for a NS, Ω_p always remains finite upto $r = 0$, except for $r = 0$ and $\theta \sim \pi/2$, i.e., near the singularity.

We obtain distinguishing characteristic features specifically in the radial profile of Ω_p for both BH and NS cases, which we will discuss as we proceed. Further, we also obtain features in the radial profile of Ω_p that could help distinguish near-extremal NSs from those with higher spin. We explore the details of such features and provide a criterion to separate near-extremal NS ($1 < a_* < 1.1$) from those with higher spins ($a_* \geq 1.1$) in Sec. VI.

We plot the modulus of the precession frequency of stationary gyros $\Omega_p = |\tilde{\Omega}_p|$, gotten from Eq.(28),

$$\Omega_p = \frac{(r^2 + a^2)^2 - a^2 \Delta \sin^2 \theta}{4q(1-q)\rho^7 \Delta} \sqrt{A^2 \Delta \cos^2 \theta + B^2 \sin^2 \theta}, \quad (51)$$

and study its variation with a_* , q , r and θ . Briefly, from the above expression, one can see that the denominator of Ω_p vanishes for $\rho = 0$, $\Delta = 0$ or $q = 0, 1$. Since it can be seen from Eq.(20) that A and B are finite valued, Ω_p becomes arbitrarily large when its denominator vanishes. $\rho = 0$ is the ring singularity, $\Delta = 0$ is the event horizon and $q = 0, 1$ are the (excluded) boundaries of the allowed values of Ω .

For a BH with $a_* = 0.9$, we can see from the left panels of Fig.2 that the precession frequency indeed becomes arbitrarily large close to the horizon for all values of a_* , q and θ , except $q = 0.5$. From panel (a), we can see that for $q < 0.5$ the radial variation of Ω_p is monotonic, with no maxima or minima. However, for $q > 0.5$, a minima starts appearing, which can be seen from panels (e) and this minima is sharp for $\theta = \pi/2$. For observers at the ZAMO frequency, $q = 0.5$, the precession frequency remains smooth and finite, as can be seen from panel (c), even for gyros orbiting close to the horizon. We note that the ZAMO frequency exhibits consistently peculiar behaviour which might lead to interesting insights on exploring further. On the other hand, for a NS with $a_* = 1.1$, as can be seen from the plots on the right in Fig.2, the spin precession frequency does not diverge. It remains finite and regular even as one approaches $r = 0$ for all angles $0 < \theta \lesssim 90^\circ$. Near $r = 0, \theta = 90^\circ$, the precession frequency becomes arbitrarily large because of the presence of the ring singularity. This is also in stark contrast to the BH case in the present paper, for which we obtain a divergence in the precession frequency close to the event horizon, ‘far away’ from $r = 0$. One also finds that a local minima and a local maxima appear for $q \geq 0.5$ for some angles, i.e. there are additional features that might help to ascertain the angular velocity of a stationary observer w.r.t. the ZAMO frequency. We also note here that it can be seen from the y -axis scales in the panels (a), (b) and (e), (f) of Fig.2 relative to the scales in the other panels that Ω_p rises sharply as the angular momentum of the stationary observer Ω nears its allowed bounding values Ω_\pm . These panels represent $q = 0.1, 0.9$ respectively for BH and NS.

In Fig.3, we demonstrate that the features obtained for $a_* = 0.9$ are characteristic to all BHs by plotting Ω_p for other values of $a_* = 0.2, 0.4, 0.6, 0.8, 1$. We show that the spin precession frequency is finite and smooth both inside and outside the ergoregion but it diverges near the horizon for all a_* , q , r and θ , except for $q = 0.5$. Finally, in Fig.4, we demonstrate that the features obtained for $a_* = 1.1$ are characteristic of NSs, in general, by considering other values of $a_* = 1.01, 1.05, 1.09, 2, 5$. We have picked these values at non-uniform intervals anticipating additional features in the plots for near-extremal NSs. We show that the spin precession frequency is finite and smooth both inside and outside of the ergoregion, same as the BH case, but it diverges near the ring singularity for all a_* , q , r and θ . This is different from the BH case, as we have already mentioned above. Indeed, we also note here that near-extremal NSs appear to have additional characteristic features which could be used to distinguish them from other generic higher spin NSs, as can be seen clearly from the panels of this figure, and we explore this observation in the following section.

We now describe our experiment to distinguish a Kerr black hole from a Kerr naked singularity. Consider gyroscopes attached to stationary observers with a non-zero azimuthal component (Ω) to their four-velocities u . These are observers moving along circles at constant r and θ , with a constant angular velocity Ω . For every orbit or trajectory at fixed (r, θ) , we can find the range of allowed $\Omega(r, \theta)$ by finding the lower and upper bounds, $\Omega_-(r, \theta)$ and $\Omega_+(r, \theta)$. We can represent this angular velocity equivalently by the parameter q , which gives the absolute relation of that observer with respect to the ZAMO ($q = 0.5$). Consider observers along two directions, say $\theta = \theta_1, \theta_2$ ($\theta_1 \approx \theta_2$). From the modulus of the precession frequencies Ω_p of gyroscopes attached to timelike

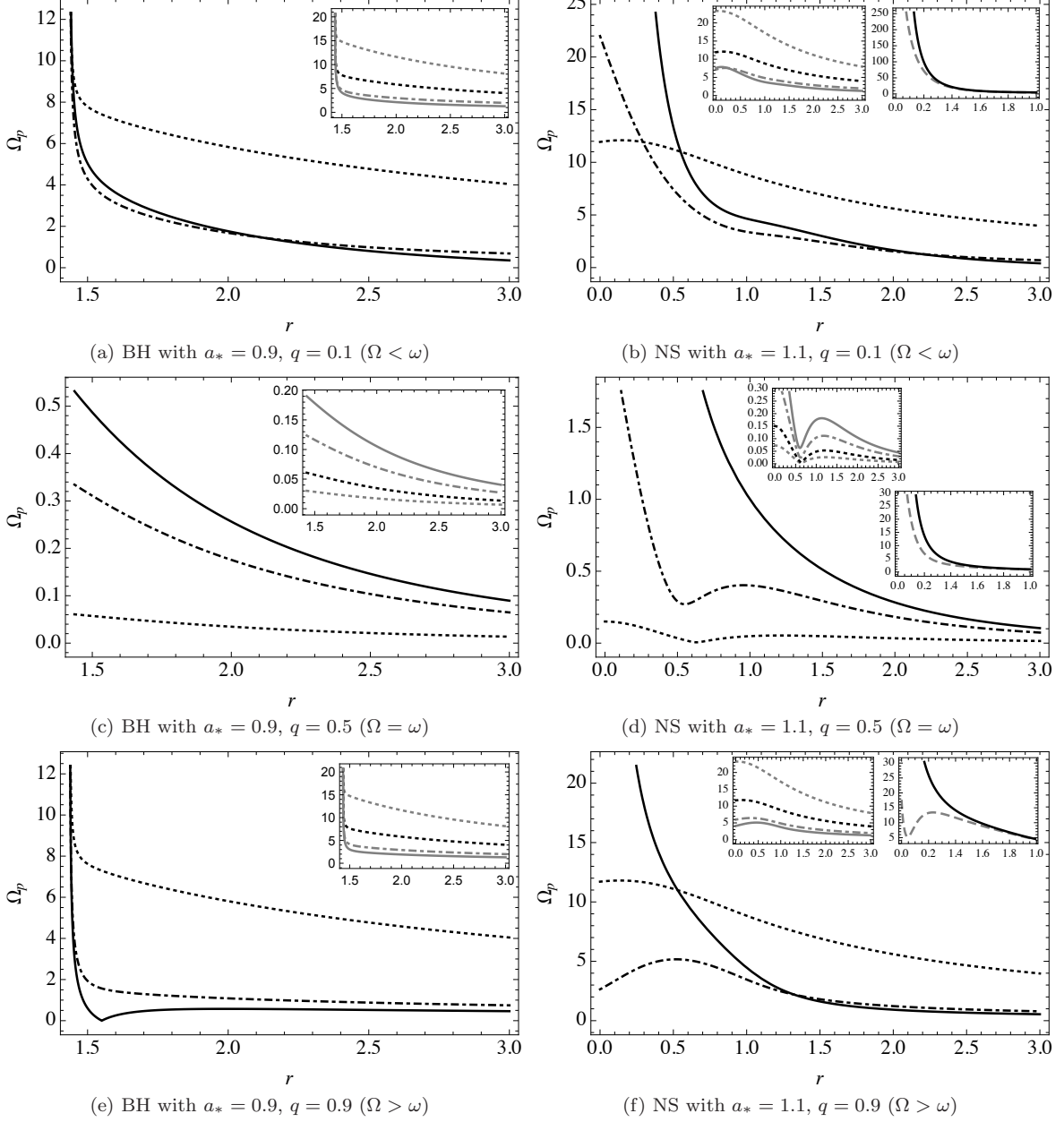


FIG. 2. We have plotted in each panel the modulus of the precession frequency of stationary gyroscopes Ω_p (in M^{-1}) versus r (in M) around a black hole (left panels) with $a_* = .9$ and a naked singularity (right panels) with $a_* = 1.1$ for different q and θ . Each of the rows has a different value of q , which measures its angular velocity, and in each panel, θ takes values $10^\circ, 50^\circ, 90^\circ$ represented in dotted black, dot-dashed black and black respectively. For the BH, r ranges from the horizon radius (which is at ~ 1.44 , in this case) to 3. For the NS, the plots begin from $r = 0$ (specifically, the singularity is at $r = 0$ and $\theta = 90^\circ$) to 3 and the ergosurface is at 2 for $\theta = 90^\circ$. It can be seen that there is a much bigger drop in Ω_p from 10° to 50° than from 50° to 90° . We have therefore inset plots (left inset for NS panels) for additional θ values (close to the pole) of $5^\circ, 20^\circ$ and 30° in dotted gray, dot-dashed gray and gray along with 10° in dotted black, same as the main panel. Further, for the NS case, since the singularity is at $\theta = 90^\circ$ in these coordinates, as $r \rightarrow 0, \theta \rightarrow 90^\circ$, the frequency blows up. We have zoomed in on the range of r between 0 and 1 and inset (on the right in the NS panels) the plots for $\theta = 80^\circ, 90^\circ$ in dashed gray and black to demonstrate how quickly Ω_p increases relative to angles much smaller than 90° .

stationary observers orbiting a Kerr compact object at different r along these two directions, we can make the

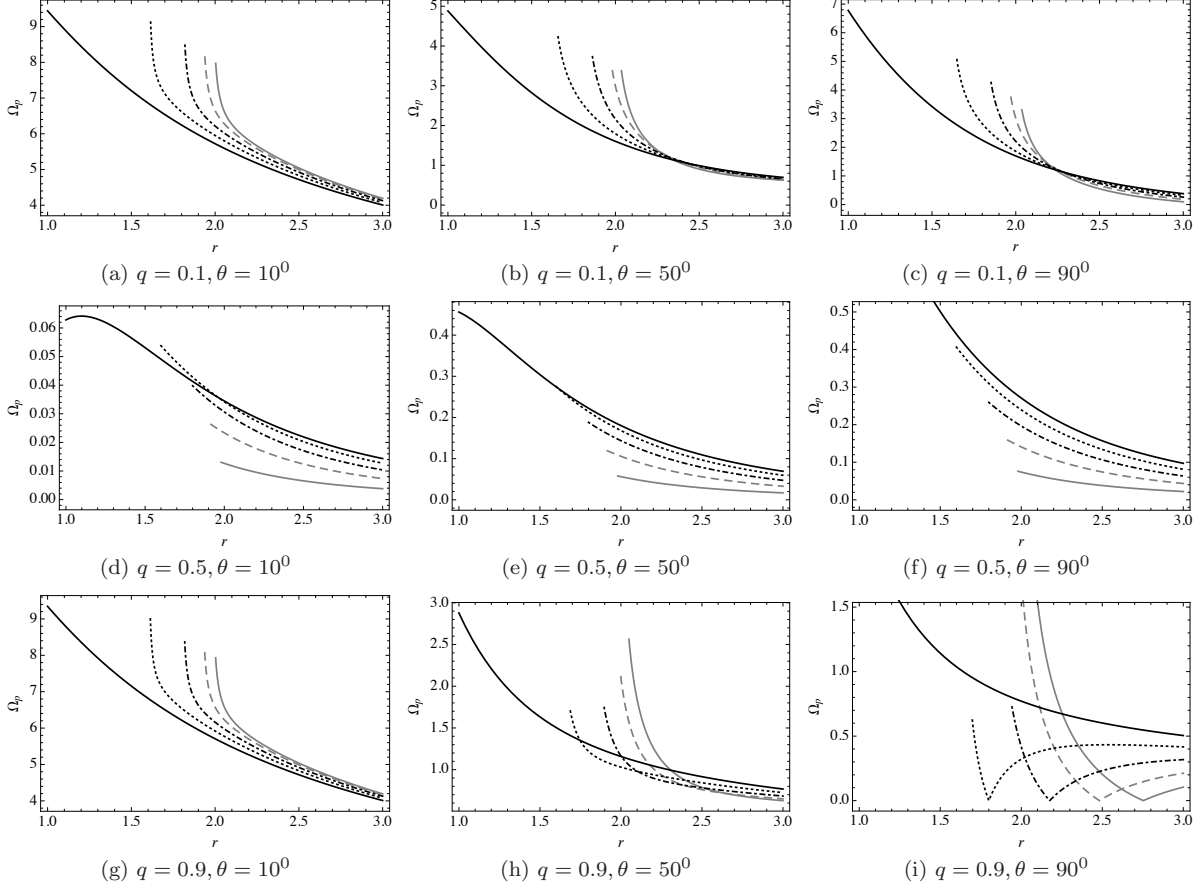


FIG. 3. We have plotted here, for black holes, the modulus of the precession frequency Ω_p (in M^{-1}) vs r (in M) for different a_* , q and θ . We have $q = 0.1, 0.5, 0.9$ in the top, middle and bottom rows respectively and $\theta = 10^\circ, 50^\circ, 90^\circ$ in the left, centre and right columns respectively. In each panel, the line style is gray, dashed gray, dot-dashed black, dotted black and black for $a_* = .2, .4, .6, .8, 1$ respectively. We have plotted Ω_p for each BH (with different a_*) between its horizon radius (r_+) and $r = 3$. The ergoregion is at $r = 2$ for $\theta = 90^\circ$ (bottom row), for reference. This figure clearly demonstrates that for all values of a_* , q , θ , the precession frequency Ω_p becomes arbitrarily large near the event horizon, in general. As can be seen from the bottom row, for $q > 0.5$, minimas appear. Specifically, from panel (i), it can be seen that the sharpness of the minimas increases with a_* , with extremal black holes as exceptions.

following statements: (i) if Ω_p becomes arbitrarily large in the limit of approach to the central object for both θ_1, θ_2 , then the spacetime contains a black hole, whereas (ii) if Ω_p becomes arbitrarily large in the limit of approach to the central object for at most one of the two directions θ_1, θ_2 , then the spacetime contains a naked singularity. The reason for this distinction is as follows. For a black hole, Ω_p becomes arbitrarily large in the limit of approach to the event horizon, which exists in all directions (i.e., for all θ) and therefore, observers approaching the black hole in all directions will display a divergence. However, for a naked singularity, since the divergence occurs only close to the ring singularity, which exists in the equatorial plane ($\theta = \pi/2$), only those observers that approach the compact object approximately along this direction will see a divergence. Therefore, if one of $\theta_1, \theta_2 = \pi/2$, then we will see a divergence only along that direction. Or, if neither $\theta_1, \theta_2 \neq \pi/2$, we will not see any divergence. Therefore, a divergence along at most one direction will indicate that the spacetime contains a naked singularity. We also note here that our statements are qualitatively independent of the mass of the compact object.

Finally, we expect that these results can possibly be extended to any black hole or naked singularity with symmetries. We have used in [3] and in this work the result that there exist invariant characterizations of ergoregions (for rotating spacetimes) and horizons respectively in terms of the Killing vectors. We set up observers equipped with gyroscopes along integral curves of these Killing vectors and then study the precession behaviour of these gyros and interpret any arbitrarily large growth in the modulus of the precession frequency that is obtained

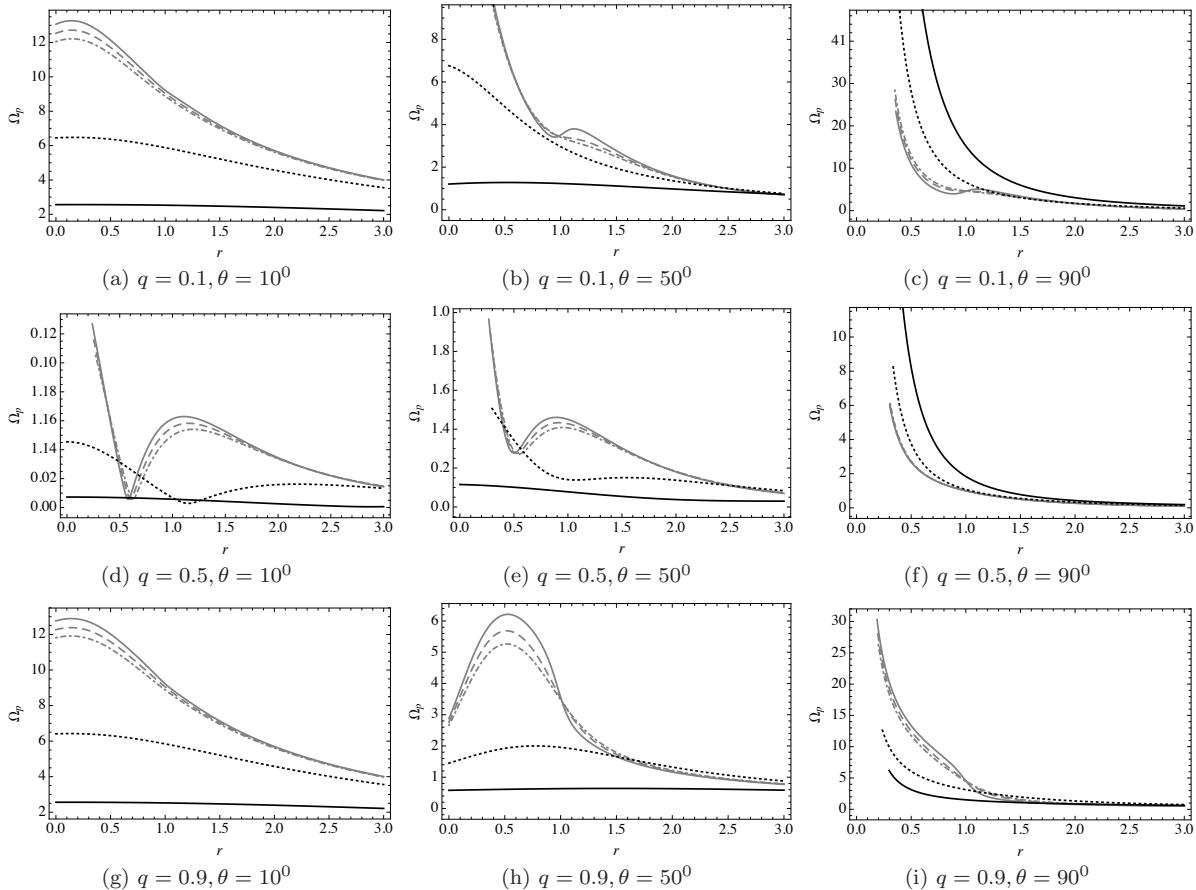


FIG. 4. We have plotted here, for naked singularities, the modulus of the precession frequency Ω_p (in M^{-1}) vs r (in M) for different a_* , q and θ . We have $q = 0.1, 0.5, 0.9$ in the top, middle and bottom rows respectively and $\theta = 10^\circ, 50^\circ, 90^\circ$ in the left, centre and right columns respectively. In each panel, the line style is gray, dashed gray, dot-dashed gray, dotted black and black for $a_* = 1.01, 1.05, 1.09, 2, 5$ respectively. We have plotted Ω_p for each NS (with different a_*) between $r = 0$ and $r = 3$. The ergoregion is at $r = 2$ for $\theta = 90^\circ$ (bottom row), for reference. This figure clearly demonstrates that for all values of a_*, q, θ , the precession frequency Ω_p becomes arbitrarily large near the ring singularity. Further, the gray lines are all near-extremal NSs and this figure demonstrates how near-extremal NSs appear to have additional characteristic features that can be used to distinguish them from NSs with higher angular momentum. Motivated thus, we explore this distinction in greater detail in Section VI since near-extremal naked singularities are of great interest from an observational standpoint, if they exist.

as indicators of the presence of an ergosurface, as in [3], or a horizon, as we have discussed here.

VI. DISTINGUISHING NEAR-EXTREMAL KERR NAKED SINGULARITIES FROM ONES WITH HIGHER ANGULAR MOMENTUM

In the previous section, we discussed how the spin precession frequency, in the case of a BH, becomes arbitrarily large at the horizon for all values of q barring $q \sim 0.5$. For a NS, it diverges only near the ring singularity $r = 0, \theta = \pi/2$ and remains finite even for $r = 0$ for $0 < \theta \lesssim \pi/2$. We pointed out that this can be used to distinguish a BH from a NS. Further, from Fig. 4, a general feature that emerges is that with increase in a_* , the radial profile of Ω_p becomes increasingly ‘smoother.’ This motivates us to use the ‘sharp’ features that appear for naked singularities with $a_* \gtrsim 1$ to separate them from those with $a_* \gg 1$. Indeed, we find that one can use the features that appear for $1 < a_* < 1.1$ to characterize them and potentially distinguish them from $a_* > 1$. In this section we highlight these features in $\Omega_p(r)$ with change in a_*, q, θ .

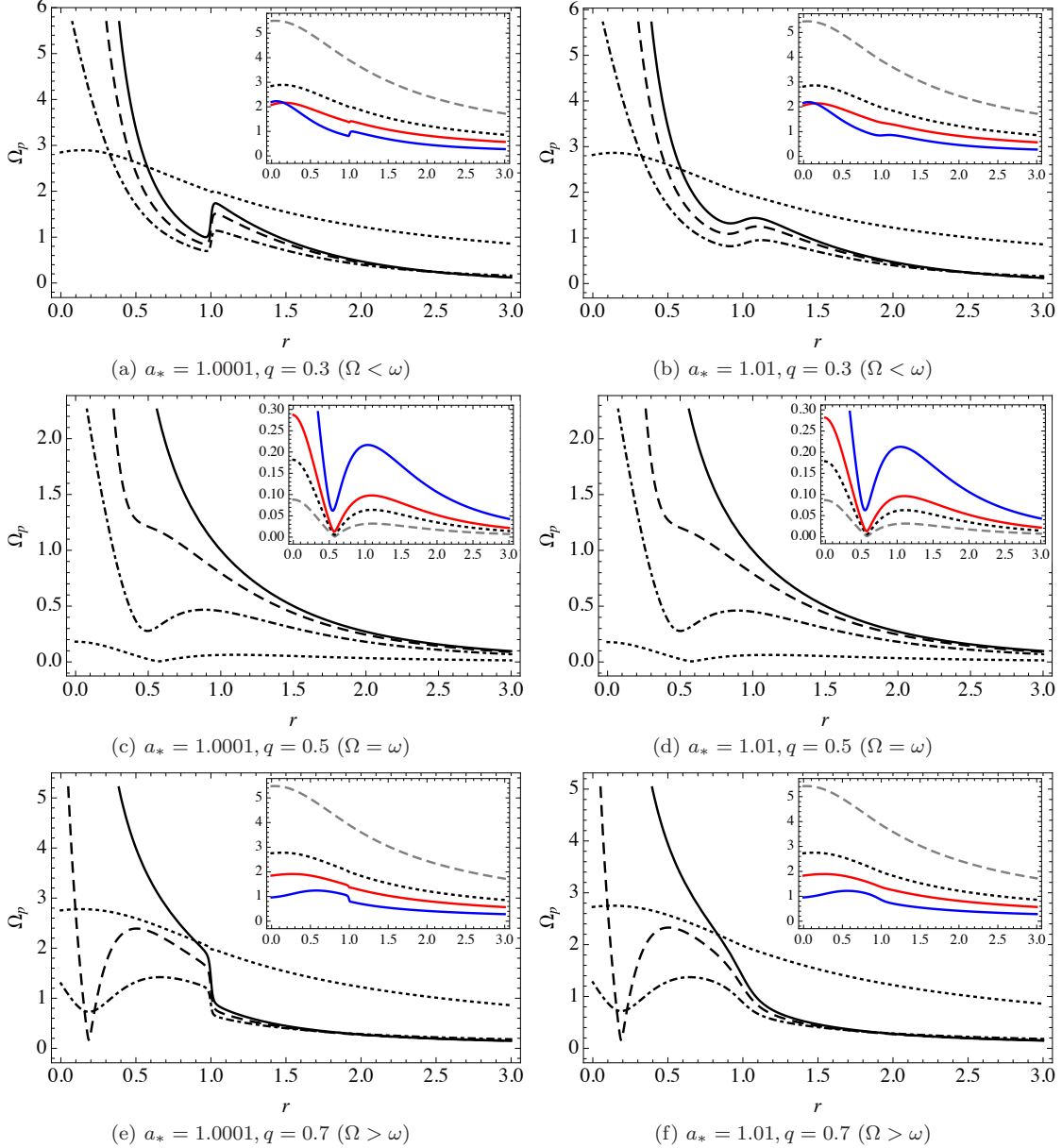


FIG. 5. The modulus of the precession frequency Ω_p (in M^{-1}) versus r (in M) has been plotted for near-extremal naked singularities with two different a_* for different q, θ . We have used $a_* = 1.0001, 1.01$ in the plots in the left and right columns and $q = 0.3, 0.5, 0.7$ in the top, middle and bottom rows, which are representative of $\Omega < \omega, \Omega = \omega$ and $\Omega > \omega$ respectively. In each panel, the black dotted, dot-dashed, dashed and regular lines represent $\theta = 10^\circ, 50^\circ, 70^\circ, 90^\circ$ respectively. This plot shows that for all q , at $\theta \sim 0^\circ$, the radial variation of Ω_p is smooth. From panels (a),(e), for $\Omega \approx \omega$, a clear maxima-minima pair appears around $r = 1$ resulting in a sharp drop/rise in Ω_p at that radius. The event horizon of an extremal black hole $a_* = 1$ is located at $r = 1$ and we link this sharp feature to this observation. At $\Omega = \omega$ itself Ω_p is smooth, devoid of this particular feature. We discuss $\Omega \sim \omega$ in the next figure since these q values have richer features. As can be seen from panels (b),(f), this sharp rise/drop in Ω_p gets smoother with increasing a_* . By $a_* \sim 1.1$, these features completely vanish and we interpret this feature as providing an important criterion based on which one can distinguish a near-extremal NS ($1 < a_* < 1.1$) from one with a higher spin. In the inset, we display approximately at what angle θ this sharp $r = 1$ feature starts to appear from and we have used $\theta = 5^\circ, 10^\circ, 15^\circ, 30^\circ$ for the gray dashed, black dotted (same as the main panel), red and blue lines respectively.

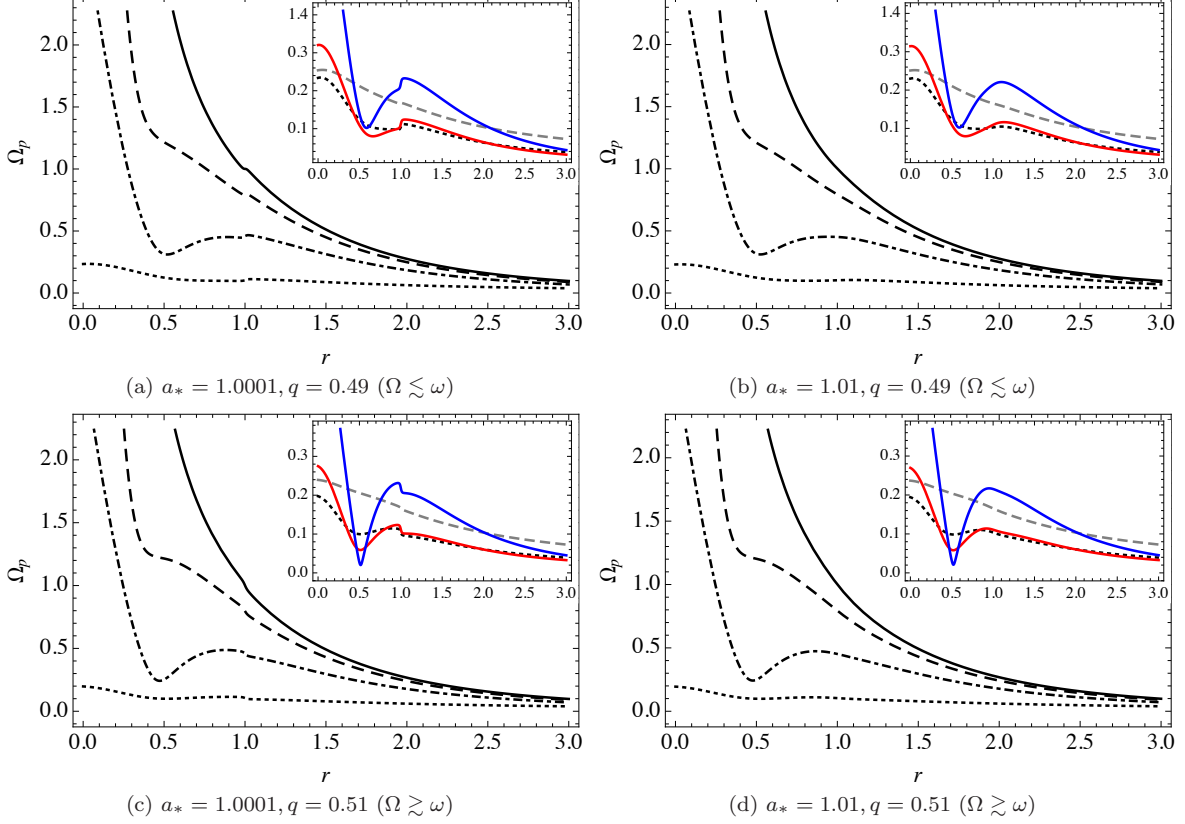


FIG. 6. We plot now Ω_p (in M^{-1}) vs r (in M) for near-extremal naked singularities with $a_* = 1.0001$ and 1.01 at different θ , for $q \sim .5$ ($q \neq .5$). The line styles are the same as Fig.5 and the insets in this figure demonstrate that for these values of q , that is q close to $.5$ but not equal to, there are richer features at smaller angles θ . It can be seen from this figure, as was from Fig.5, that with increase in a_* , these features all get smoothed out.

We lay emphasis on this study because of the importance of near extremal naked singularities in general relativity. For example, in a black hole binary collision, like the one studied by LIGO recently, the angular momentum of the compact object during the collision could temporarily exceed the Kerr bound and result in a temporary near-extremal naked singularity, a scenario that is of interest to [19]. Further, if a thick accretion disk could spin up a near extremal black hole, it would likely form a near-extremal naked singularity due to its proximity to the black hole geometry in the a_* parameter space. We mention in relation to this point that using the Polish doughnut model (not for Kerr spacetime), Li and Bambi [20] showed that the overspinning compact objects can be generated by thick accretion disks.

The radial variation of the modulus of the precession frequency for all q , at $\theta \sim 0^0$ is smooth, as can be seen from Fig.5 and Fig.6. For an observer moving with an angular velocity that is not close to the ZAMO frequency ($q \approx 0.5$), a clear maxima-minima pair appear around $r = 1$ resulting in a sharp drop/rise in Ω_p at that radius, as can be seen from panels (a) and (e) of Fig.5. The event horizon of an extremal black hole $a_* = 1$ is located at $r = 1$ and we link this sharp feature to this observation. We will discuss this in some more detail in the following subsection. Roughly, however, the reason for these sharp features is as follows. From Eq.(51), we see that Δ appears in the denominator. We know that $\Delta = 0$ marks the location of the horizon for $a_* \leq 1$ and specifically, because of this, for $a_* = 1$, Ω_p exhibits a divergence at $r = 1$. This divergence is avoided for $a_* \gtrsim 1$ since $\Delta \neq 0$ but Δ changes only slightly from 0 and hence we see a sharp change at $r \sim 1$. The dependence on θ is due to the other factors in Eq.(51). That is, $a_* \gtrsim 1$ naked singularities feel the ‘phantom effects’ of the extremal event horizon. Further, we can ascertain whether an observer is rotating with an angular frequency Ω above or below the ZAMO frequency ω , that is we can distinguish whether $\Omega > \omega$ or $\Omega < \omega$, by looking at the additional maxima-minima structure in the region $r < 1$. We note here that at $\Omega = \omega$ itself Ω_p is smooth, as can be seen

from panels (c) and (d) of Fig.5 and it is devoid of the sharp features that are obtained at $r = 1$ for $q \approx .5$. Features for $q \sim .5$ are highlighted in Fig.6.

On moving closer to the compact object, that is on decreasing r , in any direction θ , Ω_p always increases. Further, for $r \rightarrow 0$, on increasing θ , observers get closer to the ring singularity and therefore see a rapidly rising Ω_p . Specifically, as $\theta \rightarrow \pi/2$, Ω_p becomes unbounded. With increase in a_* , as is demonstrated in both Figs.5 and 6, we see that this $r = 1$ feature becomes smoother. By $a_* \sim 1.1$, these features completely vanish and we interpret this result as providing an important criterion based on which one can distinguish a near-extremal NS ($1 < a_* < 1.1$) from one with a higher spin. In the insets of both figures, we explore approximately at what angle θ this sharp $r = 1$ feature starts to appear from and this value of θ depends on a_* , in general.

A. Behavior of gyro frequency for near-extremal naked singularities

In this subsection, we will discuss the reasons for the features that are exhibited by near-extremal naked singularities that are different from those with higher spins.

Define χ from Eq.(28) for convenience as,

$$\chi = \frac{(r^2 + a^2)^2 - a^2 \Delta \sin^2 \theta}{4q(1-q) \rho^7 \Delta}, \quad (52)$$

so that the precession frequency $\vec{\Omega}_p$ becomes,

$$\vec{\Omega}_p = \chi \left[A\sqrt{\Delta} \cos \theta \hat{r} + B \sin \theta \hat{\theta} \right]. \quad (53)$$

First, we de-dimensionalise the above expression by replacing $a_* = a/M$ and introducing the dimensionless radial variable $y = r/M$. We can then write χ as,

$$\chi = \frac{(y^2 + a_*^2)^2 - a_*^2 \Delta_* \sin^2 \theta}{4q(1-q) \rho_*^7 \Delta_*} M^{-5}. \quad (54)$$

Therefore, χ has mass dimension -5 . Similarly, A and B have mass dimensions 3 and 4 respectively, $\sqrt{\Delta}$ has mass dimension 1 and the term in the square braces of Eq.(53) has a total mass dimension of 4. Therefore, $\vec{\Omega}_p$ has an overall mass dimension of -1 . In this section, henceforth, we work exclusively with dimensionless quantities and simply drop all factors of M . We write down now the dimensionless expressions for a near-extremal NS by replacing $a_* = 1 + \epsilon$ ($\epsilon > 0$),

$$\chi_{\text{ne}} = \frac{(y^2 + 1 + 2\epsilon)^2 - (1 + 2\epsilon)\Delta_{\text{ne}} \sin^2 \theta}{4q(1-q)\rho_{\text{ne}}^7 \Delta_{\text{ne}}}, \quad (55)$$

$$A_{\text{ne}} = 2(1 + \epsilon)y - \frac{\Omega_{\text{ne}}}{8} \left\{ 8y^4 + 8(1 + 2\epsilon)y^2 + 16(1 + 2\epsilon)y + 3(1 + 4\epsilon) \right.$$

$$\left. + 4(1 + 2\epsilon)(2\Delta_{\text{ne}} - 1 - 2\epsilon) \cos 2\theta + (1 + 4\epsilon) \cos 4\theta \right\} + 2\Omega_{\text{ne}}^2 (1 + 3\epsilon)y \sin^4 \theta,$$

$$B_{\text{ne}} = (1 + \epsilon)(y^2 - (1 + 2\epsilon) \cos^2 \theta) + \Omega_{\text{ne}} \left\{ (1 + 4\epsilon)y \cos^4 \theta + y^2(y^3 - 3y^2 - (1 + 2\epsilon)(1 + \sin^2 \theta)) \right.$$

$$\left. + (1 + 2\epsilon) \cos^2 \theta (2y^3 - y^2 + (1 + 2\epsilon)(1 + \sin^2 \theta)) \right\}$$

$$+ \Omega_{\text{ne}}^2 (1 + \epsilon) \sin^2 \theta [y^2(3y^2 + 1 + 2\epsilon) + (1 + 2\epsilon) \cos^2 \theta (y^2 - 1 - 2\epsilon)],$$

$$\Omega_{\text{ne}} = \frac{2(1 + \epsilon)y \sin \theta - (1 - 2q) \rho_{\text{ne}}^2 \sqrt{\Delta_{\text{ne}}}}{\sin \theta [\rho_{\text{ne}}^2 (y^2 + 1 + 2\epsilon) + 2(1 + 2\epsilon)y \sin^2 \theta]},$$

$$\Delta_{\text{ne}} = y^2 - 2y + 1 + 2\epsilon,$$

$$\rho_{\text{ne}}^2 = y^2 + \cos^2 \theta + 2\epsilon \cos^2 \theta$$

where subscript ‘ne’ stands for ‘near-extremal.’ For some constant κ , we can write,

$$\begin{aligned} (\Delta_{\text{ne}})^\kappa &\approx (y-1)^{2\kappa} \left[1 + \epsilon \frac{2\kappa}{(y-1)^2} \right], & \text{if } |y-1| \gg \epsilon \\ &\approx \epsilon^\kappa, & \text{otherwise,} \\ (\rho_{\text{ne}}^2)^\kappa &\approx (y^2 + \cos^2 \theta)^\kappa \left[1 + \epsilon \frac{2\kappa \cos^2 \theta}{y^2 + \cos^2 \theta} \right], & \text{if } |y^2 + \cos^2 \theta| \gg \epsilon \\ &\approx (\epsilon \cos^2 \theta)^\kappa, & \text{otherwise.} \end{aligned} \quad (56)$$

$y = 1$ was the location of the event horizon for an extremal black hole ($a_* = 1$), which vanished as a_* was changed slightly from 1. As can be seen from the above expressions, this is a special point for Δ_{ne} . For ρ_{ne} , the two cases correspond to being far from and near the ring singularity at $r = 0, \theta = \pi/2$ respectively.

As can be seen from Eq.(55), Ω_{ne} is finite and smooth always (remember that at the pole i.e., for $\theta = 0$, the only allowed value of Ω is $\Omega = 0$ and hence, $\Omega_{\text{ne}, \theta=0} = 0$). Therefore, A and B are also finite and smooth and we can restrict ourselves to studying χ_{ne} to find any interesting ‘sharp’ features in the radial profile of the modulus of the precession frequency Ω_p , for a near-extremal NS. Indeed, we can see from χ_{ne} given in Eq. (55) that the factor of Δ_{ne} in the denominator will drive Ω_p to rise sharply near $y = 1$ for near-extremal naked singularities. Specific maxima/minima structure in the radial profile of Ω_p can also be ascertained from Eq.(55).

B. Near-extremal overspinning Kerr geometry and ultra-high energy collisions

Many interesting physical processes occur in near-extremal Kerr geometry at $r = M$. These processes include ultra-high energy particle collisions and collisional Penrose process with extremely large efficiency of energy extraction.

In [21, 22], we considered two particles which follow geodesic motion on the equatorial plane of overspinning Kerr geometry starting from rest at infinity and undergo a collision at $r = M$. One of the particles that is initially ingoing, turns back at radial coordinate $0 < r < M$ and appears at $r = M$ as an outgoing particle, while the second particle is ingoing. We showed that the center of mass energy of collision between the radially ingoing and outgoing particles shows divergence in the near-extremal limit where Kerr spin parameter transcends the extremal value by an infinitesimal amount, i.e., $a = M(1 + \epsilon)$ with $\epsilon \rightarrow 0^+$. This process overcomes many limitations and finetunings involved in an analogous high-energy collision process between the two ingoing particles which occurs close to the event horizon of the maximally spinning BH [23, 24].

We further showed that the particles which are produced in the ultra-high energy particle collisions in the overspinning Kerr spacetime can escape to infinity with divergent energies [25]. This is a consequence of the collisional Penrose process which allows us to extract rotational energy from the ergoregion of the Kerr spacetime. The efficiency of the collisional Penrose shows divergence in the near-extremal limit for the collisions which occur at $r = M$, making it possible to extract large amount of energy from the overspinning Kerr geometry. This is in the stark contrast with the BH case where efficiency is shown to be always finite with an upper bound of 14 [26]. Thus near-extremal NS spacetime can possibly be the source of the ultra-high energy cosmic rays and neutrinos.

Interestingly, as we showed earlier in this section, gyro precession frequency shows a sharp increase or decline close to $r = M$ in near-extremal overspinning Kerr spacetime as we decrease its radial coordinate along the constant value of θ . This is precisely the location where ultra-high energy collisions and collisional Penrose process with divergent efficiency occurs. Thus a thought experiment to lower gyro which we described in this paper kills two birds with the same bullet. Firstly it allows us to identify the spacetime geometry which is conducive to the high-energy processes as it can tell us whether the geometry is overspinning and near-extremal. Secondly it also helps us to locate region in space which can host high-energy processes as gyro frequency exhibits peculiar trend exactly at this location. This coincidence is quite remarkable.

VII. FRAME-DRAGGING EFFECT IN ACCRETION DISKS IN A KERR GEOMETRY

In order to study the accretion disk around a spinning BH, one needs to study the stable circular orbits in the Kerr space-time. The last or innermost stable circular orbit (ISCO) marks the inner boundary of this disk. The ISCO radius depends on the Kerr parameter a_* , as shown in FIG. 7. This is a key underlying physical feature that can distinguish BHs from NSs, as we will see in this section.

The three fundamental frequencies for the accretion disk, namely the Keplerian frequency Ω_ϕ , vertical epicyclic frequency Ω_θ , and the radial epicyclic frequency Ω_r are derived for the Kerr metric [27, 28] (in geometrized units)

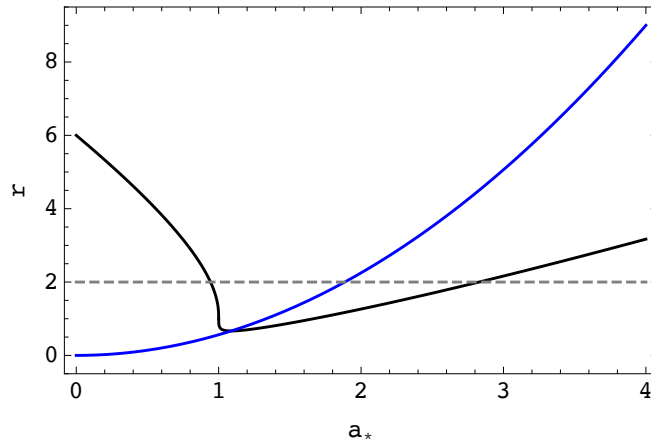


FIG. 7. Three radial quantities (in units of M) for prograde orbits, namely the ISCO radius (black), the ergoradius (dashed gray), and the radius (r_0) at which the precession frequency (Ω_{nod}) vanishes (blue), plotted as functions of the dimensionless Kerr parameter $a_* = a/M$. The ISCO radius lies outside the ergoregion for all a_* except $0.943 \leq a_* \leq 2.838$. r_0 meets the ISCO radius at $a_* = 1.089$. This has the implication that for smaller values of a_* , the LT frequency is always positive and does not vanish for any radius. For larger values, there is a domain of r for which this frequency becomes negative, signifying that the LT effect switches sign. Since this feature is exhibited for $a_* = 1.089 > 1$, the LT frequency in a BH spacetime never vanishes. We point out that NSs with $a_* < 1.089$ also do not display vanishing LT frequency.

as,

$$\Omega_\phi = \pm \frac{M^{\frac{1}{2}}}{(r^{\frac{3}{2}} \pm aM^{\frac{1}{2}})} \quad (57)$$

$$\Omega_r = \Omega_\phi \left(1 - \frac{6M}{r} \pm \frac{8aM^{\frac{1}{2}}}{r^{\frac{3}{2}}} - \frac{3a^2}{r^2} \right)^{\frac{1}{2}} \quad (58)$$

$$\Omega_\theta = \Omega_\phi \left(1 \mp \frac{4aM^{\frac{1}{2}}}{r^{\frac{3}{2}}} + \frac{3a^2}{r^2} \right)^{\frac{1}{2}} \quad (59)$$

where the upper sign is applicable for direct orbit and the lower one for retrograde orbit. These frequencies are related to the precession of the orbit and orbital plane. Precession of the orbit is measured by the periastron precession frequency (Ω_{per}), and orbital plane precession is measured by the nodal plane precession or Lense-Thirring precession frequency (Ω_{nod}) [29]. These two frequencies are defined as [30]

$$\Omega_{\text{per}} = \Omega_\phi - \Omega_r, \quad (60)$$

$$\Omega_{\text{nod}} = \Omega_\phi - \Omega_\theta. \quad (61)$$

Orbital plane precession arises only due to the rotation of the spacetime. In a non-rotating spacetime, Ω_ϕ is always equal to Ω_θ , and hence the Lense-Thirring precession is entirely absent. However, periastron precession occurs both in rotating and non-rotating spacetimes. We note that the square of the radial epicyclic frequency Ω_r^2 vanishes at the ISCO, and is negative for smaller radii, which shows a radial instability for such orbits. Outside the ISCO, Ω_r^2 is always positive and Ω_θ^2 is always non-zero and positive in a rotating spacetime. The same cannot be said about Ω_{nod} . For example, the LT precession frequency (Eq.(61)) can be zero at $r = r_0$ given by,

$$\Omega_{\text{nod}}(r_0) = 0 \Rightarrow r_0 = \frac{9}{16} a_*^2 M = 0.5625 a_*^2 M. \quad (62)$$

Since r_0 is always less than r_{ISCO} ($6M \geq r_{\text{ISCO}} \geq M$ [15]) and even inside the event horizon for a BH ($0 \leq a_* \leq 1$), the LT precession frequency never becomes zero for a BH spacetime. We now discuss the location of the ISCO in a NS spacetime and argue that its relation with r_0 has implications for distinguishing BH and NS spacetimes.

FIG. 7 shows that the ISCO radius decreases with increasing a_* for prograde orbits for both BHs and NSs up to $a_* = \sqrt{32/27} \approx 1.089$, and then increases [31–33]. Therefore, the minimum ISCO radius, having the value

$r_{\text{ISCO}} = 2M/3$, occurs for $a_* = 1.089$. As seen from FIG. 7, the ISCO lies on or inside the ergosurface for $0.943 \leq a_* \leq 2.838$. For each a_* value, there exists a radius (r_0) at which there is no frame-dragging effect, and hence the LT precession vanishes. This radius is less than the ISCO radius for $a_* < 1.089$ (FIG. 7), but this may not be observationally important, as the accretion disk extends up to r_{ISCO} . FIG. 7 also shows that r_0 equals r_{ISCO} for $a_* = 1.089$ [34], and is greater than r_{ISCO} for $a_* > 1.089$. These make 1.089 a special value of a_* .

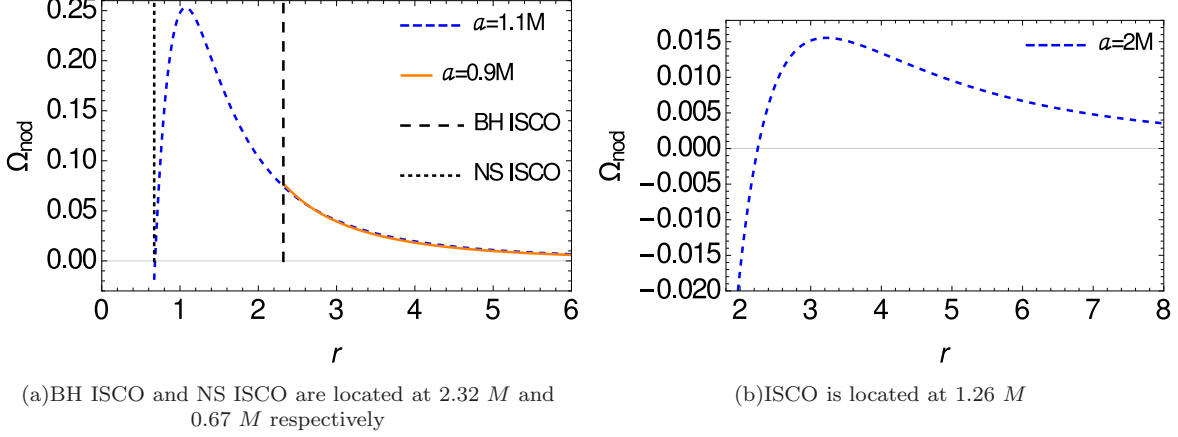


FIG. 8. Variation of Ω_{nod} (in units of M^{-1}) versus r (in units of M). It is seen from the plots that nodal plane precession frequency Ω_{nod} always increases as one approaches a BH but in case of a NS, we obtain a peak value of Ω_{nod} for all $a_* > 1$. Ω_{nod} vanishes in a particular orbit of radius r_0 for $a_* \geq 1.089$ and it becomes negative (which means that the LT precession reverses direction) in all the orbits which are in the range $r_0 > r \geq r_{\text{ISCO}}$ for $a_* > 1.089$.

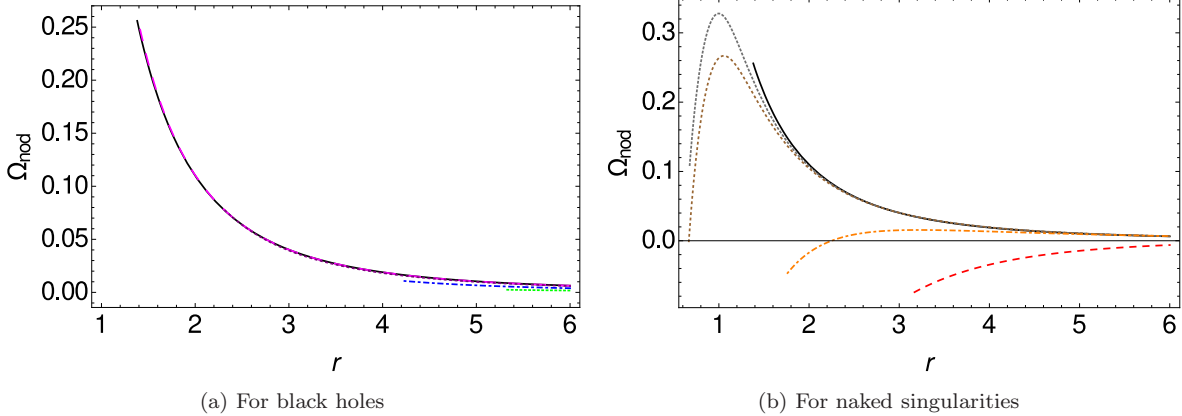


FIG. 9. We show the radial variation of the precession frequency (Ω_{nod}) (in units of M^{-1}) for different a_* BHs in the left panel and NSs on the right panel. For BHs, we plot Ω_{nod} between their respective ISCO radii and $r = 6$. We have used $a_* = 1$ (black), .9999 (large dashed, magenta), .9 (dotted, purple), .5 (dot-dashed, blue) and .2 (tiny dashed, green). Ω_p decreases with increasing r always for BHs. For NSs, we plot Ω_{nod} between their respective ISCO radii and $r = 6$. We have included also the extremal BH case to demonstrate the clear change in characteristic features. We have used $a_* = 1$ (black), 1.05 (tiny dashed, gray), 1.089 (dotted, brown), 2 (dot-dashed, orange), 4 (medium dashed, red). For NSs, as we increase r , Ω_{nod} always increases initially at the ISCO radius, reaches a peak value and decreases. Negative Ω_{nod} implies that the sense of precession has changed. These are characteristic features of NSs.

In case of BHs, the LT frequency increases with decreasing r up to the inner edge of the accretion disk (see FIG. 8 and Panel (a) of FIG. 9). But for NSs, the LT frequency attains a maximum at $r = r_p$ which occurs always at $r(r = r_p) > r_{\text{ISCO}}$ (see TABLE I), and then decreases as r decreases (FIG. 8 and Panel(b) of 9). As shown in FIGs. 7, 8 and Panel (b) of 9, the LT precession frequency becomes negative for $r_{\text{ISCO}} \leq r < r_0$, in case of $a_* > 1.089$. This means that the direction of LT precession is reversed. The maximum value of $\Omega_{\text{nod}} (= 1/2M)$

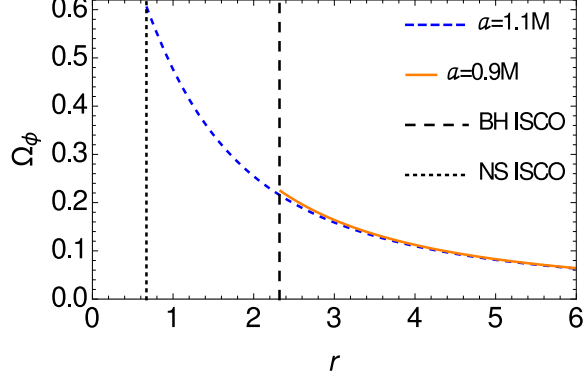


FIG. 10. Variation of Ω_ϕ (in units of M^{-1}) versus r (in units of M). BH ISCO and NS ISCO are located at $2.32 M$ and $0.67 M$ respectively. The plots show that Kepler frequency Ω_ϕ for a NS is much higher than for a BH at their respective ISCOs for $\epsilon = \pm 0.1$, i.e., $a_* = 0.9$ and $a_* = 1.1$. The difference between the values of Kepler frequencies of a NS and a BH decreases with decreasing the value of ϵ .

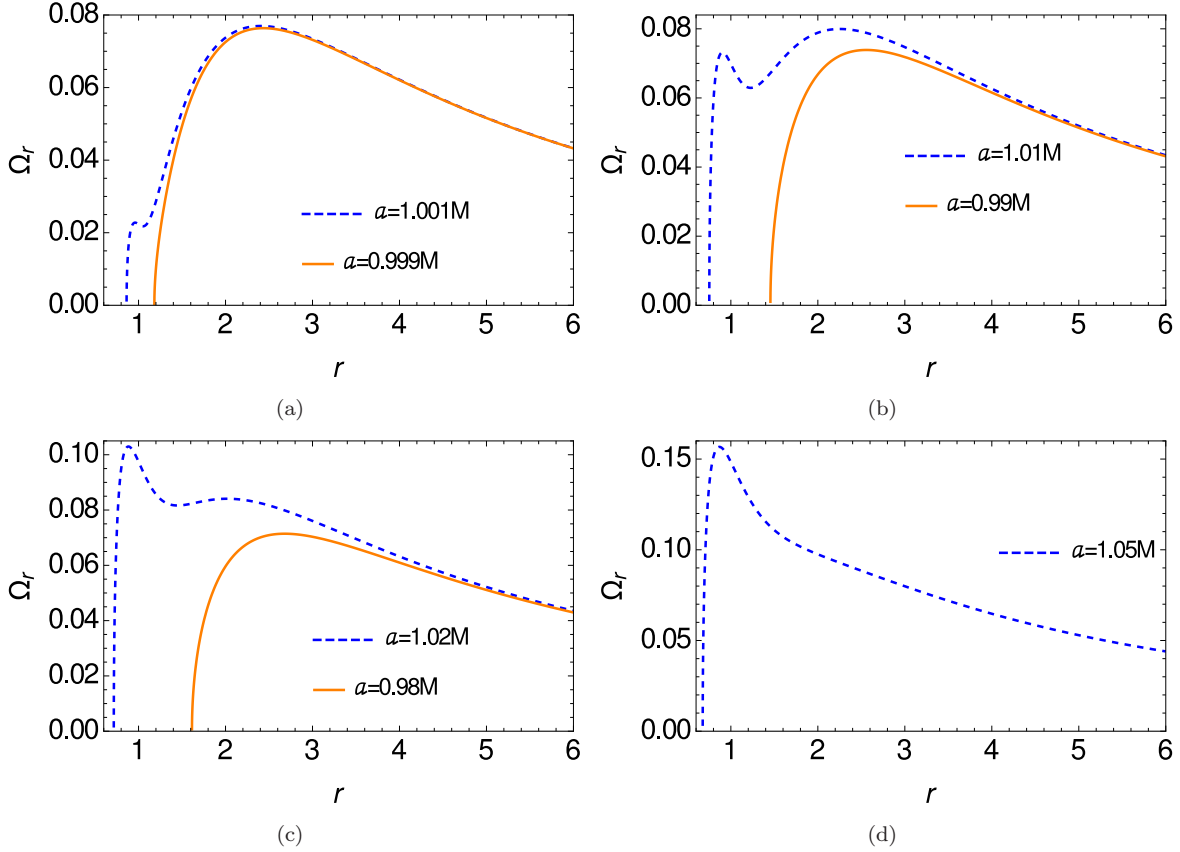


FIG. 11. Variation of Ω_r (in units of M^{-1}) versus r (in units of M). The plots show that Ω_r vanishes at their respective ISCOs of a BH and a NS, which is expected but it can be seen that a small ‘kink’ appears in some of these near-extremal NS cases. This feature is quite clear for $a_* \gtrsim 1.001$ and it disappears for $a_* = 1.05$.

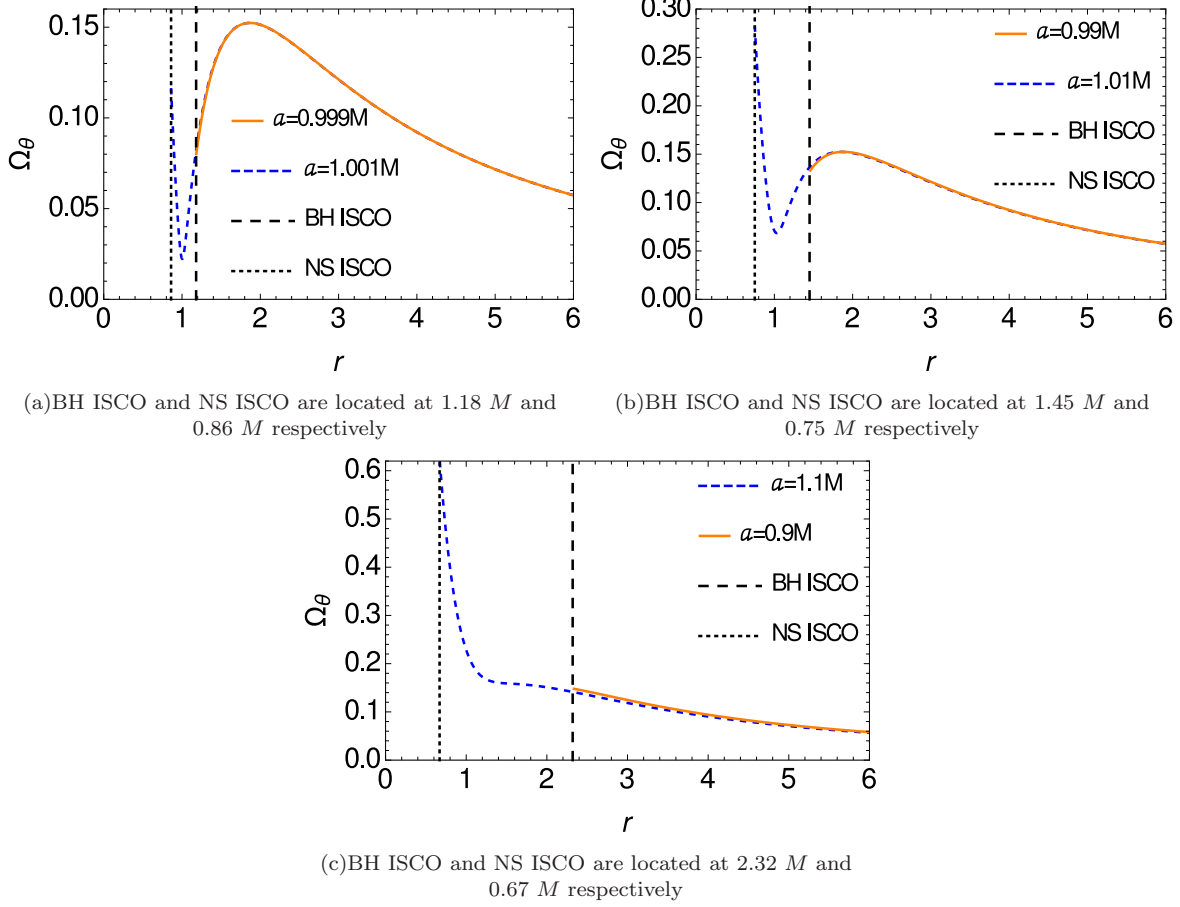


FIG. 12. Variation of Ω_θ (in units of M^{-1}) versus r (in units of M). The plots show that a local minima is always appeared outside of the ISCO for $1 < a_* < 1.1$ in Ω_θ curves, in principle. This feature is completely absent in the case of a BH.

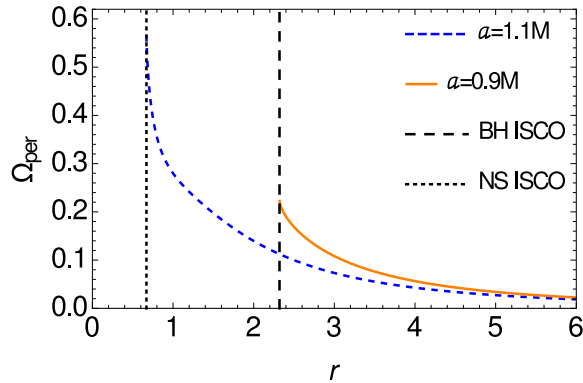


FIG. 13. Comparison between the periastron precession frequencies (Ω_{per} in units of M^{-1}) of a BH and a NS at their respective ISCOs for $\epsilon = \pm 0.1$. BH ISCO and NS ISCO are located at $2.32 M$ and $0.67 M$ respectively.

a_*	r_{ISCO} (in M)	ν_ϕ (in Hz)	ν_θ (in Hz)	ν_{nod} at r_{ISCO} (in Hz)	ν_{nod} (in Hz) at r_p (mentioned in parentheses)
0.1	5.67	234	231	3	
0.2	5.32	255	247	8	
0.3	4.98	279	265	14	
0.4	4.61	309	287	22	
0.5	4.23	346	312	34	
0.6	3.82	395	342	53	
0.7	3.39	458	378	80	
0.8	2.91	552	421	131	
0.9	2.32	718	472	246	
0.98	1.61	1053	462	590	
0.99	1.45	1163	420	743	
0.999	1.18	1395	252	1142	
0.9999	1.07	1510	118	1392	
0.99999	1.03	1556	54	1502	
0.999999	1.016	1572	30	1542	
1.0	1	1591	0	1591	
1.000001	0.98	1615	40	1575	1586 (.998)
1.00001	0.96	1640	84	1556	1584 (.994)
1.0001	0.93	1677	157	1520	1571 (.992)
1.001	0.86	1769	370	1399	1528 (.976)
1.01	0.75	1918	900	1017	1367 (.952)
1.02	0.71	1967	1199	768	1261 (.962)
1.04	0.68	1988	1538	450	1104 (.976)
1.06	0.67	1979	1745	234	1004 (.984)
1.08	0.667	1959	1894	65	886 (1.04)
$\sqrt{32/27}$ ≈ 1.089	2/3	1949	1949	0	847 (1.05)
1.1	0.67	1935	2013	-77	804 (1.07)
2	1.26	932	1588	-655	49 (3.2)
4	3.17	330	566	-236	2 (12.3)
6	5.38	172	288	-116	0.25 (27.7)

TABLE I. An object of mass $M = 10M_\odot (= 15 \text{ km})$ has been considered to calculate ν_ϕ (Kepler frequency), ν_θ (vertical epicyclic frequency) and ν_{nod} (nodal plane precession frequency) using Eq.(57) and Eq.(59). For an example, the conversion factor between ν_ϕ and Ω_ϕ is as follows : ν_ϕ (in kHz) = Ω_ϕ (in km^{-1}) $\cdot \frac{300}{2\pi M}$, and so on. For other values of M , the values of $\nu_\phi, \nu_\theta, \nu_{\text{nod}}$ (column no. 3, 4, 5 & 6) of the table have to be multiplied by $10M_\odot/M$. The values in the parentheses of Column no. 6 show the position of the peak of ν_{nod} .

occurs for $a_* = 1$ at $r = r_{\text{ISCO}}$. We also note that

$$\left. \frac{d\Omega_{\text{nod}}}{dr} \right|_{r_{\text{ISCO}}} < 0 \text{ for BH,} \quad (63)$$

$$\left. \frac{d\Omega_{\text{nod}}}{dr} \right|_{r_{\text{ISCO}}} > 0 \text{ for NS,} \quad (64)$$

and hence Ω_{nod} decreases (increases) with r at r_{ISCO} for BHs (NSs).

The profiles of other frequencies, i.e., Ω_ϕ , Ω_r , Ω_θ and Ω_{per} , can also show differences between BHs and NSs. FIG. 10 shows that Ω_ϕ behaves similarly for BHs and NSs, but much larger values are possible for the latter, simply because the disk can extend up to much lower radii. FIG. 11 shows that a small additional peak appears in the plot of Ω_r profile for the near extremal value of a_* in the case of a NS. Such a peak appears at small radius values, where an accretion disk cannot exist in case of a BH. As a_* increases, this peak becomes more prominent for $a_* = 1.01$ and it becomes the only peak for $a_* \sim 1.05$. Such an additional peak does not appear for the case of a BH. Similarly, a minimum occurs in the Ω_θ profiles for NSs with $1 < a_* < 1.1$ near the radius $r = M$ (FIG. 12). Such a minimum does not occur for a BH. Besides, Ω_θ for a_* roughly above 1.01 can attain a much higher value than that for BHs. Finally, the periastron precession frequencies for NSs can attain values much higher than those for BHs (FIG.13).

Observational aspects

BH X-ray binary (BHXB) sources show a plethora of timing features in X-rays [35]. Most notable among them are high-frequency (HF) quasi-periodic oscillations (QPOs) and three types of low-frequency (LF) QPOs. Sometimes two HF QPOs are seen together. Their frequencies are observed to be in the range of several tens to several hundreds of Hz. For example, while XTE 1650–500 has shown HF QPOs in the range of 50 – 270 Hz, 4U 1630–47 has shown such QPOs in 150 – 450 Hz [36]. The three LF QPOs are denoted with types ‘A’, ‘B’ and ‘C’, and their frequencies are typically in the ranges 6.5 – 8 Hz, 0.8 – 6.4 Hz and 0.01 – 30 Hz respectively. While several models exist to explain these QPOs, they are often associated with the relativistic precession (RP) of the accretion disk, and hence with the frequencies Ω_ϕ , Ω_r , Ω_θ , Ω_{per} and Ω_{nod} . The RP model was originally conceived to explain the twin kilo-Hertz (kHz) QPOs and a low-frequency QPO of neutron star low-mass X-ray binaries [37, 38]. Following this idea, frequencies of the C-type LF QPO, the lower frequency HF QPO and the higher frequency HF QPO of BHXBs are identified with Ω_{nod} , Ω_{per} and Ω_ϕ respectively [39]. This can be useful to measure both the mass (M) and a_* of the compact object, as demonstrated by [40]. Table I shows that the observed LF QPOs could be identified with Ω_{nod} only for $a_* < 0.5$ and $a_* \sim 1.089$ (see also [41]). In fact, Ω_{nod} could have a much higher value for a_* closer to 1 for both BH and NS, and it could be possible to identify an HF QPO with Ω_{nod} (Table I). If a_* is very close to 1, Ω_{nod} value is quite high (Table I), and such high frequency QPOs could be detected in future for BH and NS with $a_* \approx 1$. While there are uncertainties in the specific identifications of observed frequencies with the theoretical ones, the recent discovery of the C-type quasi-periodic variation of the broad relativistic iron line energy from the BHXB H1743–322 strongly suggests that the inner accretion disk of this source is indeed tilted and precessing [42]. Therefore, the theoretical dependencies of various frequencies on a_* , as discussed in this section, have potential to distinguish between a BH and a NS.

How could this be done? Here we give some examples. Note that most of the BHXBs are transient sources, and an accretion disk is formed only during an outburst. Even for the persistent BHXBs, source state often changes, which implies changes in accretion components. So it is expected that the accretion disk of a given BHXB sometimes advances towards the central object, and sometimes recedes, depending on the source intensity and spectral states. If QPOs are connected to the natural frequencies mentioned above, then such a dynamics of the disk would mean changes in QPO frequencies, as these frequencies depend on the radial distance. And we do observe evolution of QPO frequencies. As a BH and a NS have significantly different theoretical radial profiles of frequencies, it could be, in principle, possible to distinguish them by tracking the evolution of QPO frequencies as the disk advances or recedes. For example, Ω_{nod} for a BH will monotonically increase, and will attain the maximum value, if the disk advances up to the ISCO radius. But Ω_{nod} for a NS will first increase, will attain the maximum value, and then will decrease, as the disk advances up to r_{ISCO} , which can be quite different from the r_{ISCO} of BHs. In fact, in case of a NS, the absolute value of Ω_{nod} can become zero and then increase again. Whether this will happen, and radial locations of the maximum and zero values of Ω_{nod} depend on a_* . Therefore, the Lense-Thirring precession can provide a way to distinguish between a BH and a NS. Similarly, the maximum possible value of Ω_ϕ depends on a_* . Finally, according to the above mentioned model, Ω_r is interpreted as the separation between two HF QPO frequencies. Therefore, the qualitatively different Ω_r radial profiles for NSs with $a_* \lesssim 1.05$ can be useful to distinguish them from BHs.

VIII. CONCLUSION

The precession frequencies of the spin of test gyros attached to timelike stationary observers in the BH case are finite both in and outside of the ergoregion but become arbitrarily large as one considers a gyro located in an orbit close to the horizon, $r \sim r_+$, in any direction ($0 < \theta \leq \pi/2$). In contrast to this, for NS, the precession frequencies of such gyros remain finite and regular even if one considers those close to $r = 0$, for all $\theta \approx \pi/2$. Since the ring singularity itself is present at $r = 0, \theta = \pi/2$, the gyro frequency diverges in the limit of approach to this region. For gyros placed increasingly closer to a BH or NS in the equatorial plane, their precession frequencies diverge in both the cases in different ways, that is, it diverges close to the horizon in the case of BH whereas the divergence occurs close to $r = 0$ for NS.

Interestingly, we have shown that the spin precession frequency stays finite in the limit of approach to the horizon for a zero angular momentum observer (ZAMO) ($q = 0.5$) and diverges in all other cases. Further, we have shown that a sharp rise/fall in the modulus of the precession frequency is a tell-tale indication of the existence of a near extremal naked singularity and the location of this feature is at $r = M$. The specific maxima/minima structure in the radial profile of the modulus of the precession frequency Ω_p for a near extremal naked singularity

(for example, two local maxima or two local minima or two peaks or three peaks with a plateau etc) would indicate how fast the observer is moving with respect to the ZAMO frequency.

As we find, the nodal plane precession frequency, related to the accretion disc, has distinctive features that can be used to characterize both black holes and naked singularities, and we summarize them here. We can use these features to potentially make a statement regarding the existence of a NS: (i) A maxima or a peak is obtained for Ω_{nod} at some $r = r_p(a_*)$ for all $a_* > 1$, indicating the existence of a NS. (ii) Ω_{nod} vanishes at $r = r_0$ for a NS with $a_* \geq 1.089$ and becomes negative (which means that the LT precession reverses direction) in all orbits with $r_0 > r \geq r_{\text{ISCO}}$, for a NS with $a_* > 1.089$. (iii) Additionally, Ω_{nod} shows a ‘peculiar’ effect: $\Omega_{\text{nod}} \propto r^n$ (where $n \gtrsim 0$, see FIG.8) in the region $r_0 \leq r < r_p$. This curve does not follow the inverse cube law of distance like other astrophysical objects. All these features are completely absent in the case of BH and this would be reflected in the observation of frequencies of QPOs.

Finally, it can be seen from FIG.11 and FIG.12 that Ω_r and Ω_θ also have characteristic differences [43] in the cases of BH and NS by which it may be possible to detect a NS if Ω_r and Ω_θ are the observationally measurable quantities [44]. It follows that if all of the above mentioned features are never observed, then we can conclusively state that Kerr naked singularities do not exist, or at least their abundance may be extremely small.

Acknowledgments: We thank the referee for the valuable comments and suggestions. MP acknowledges support from the NCN grant Harmonia 6 (UMO2014/14/M/ST9/00707).

-
- [1] <http://www.eventhorizontelescope.org/>
 - [2] C. Chakraborty, P. Majumdar, *Class. Quantum Grav.* **31**, 075006 (2014)
 - [3] C. Chakraborty, P. Kocherlakota, P. S. Joshi, *Phys. Rev. D* **95**, 044006 (2017)
 - [4] P. S. Joshi, D. Malafarina, R. Narayan *Class. Quantum Grav.* **31**, 015002 (2014)
 - [5] D. Bini, A. Geralico, R. T. Jantzen, *Phys. Rev. D* **94**, 064066 (2016)
 - [6] D. Bini, A. Geralico, R. T. Jantzen, arXiv:1610.06513 [gr-qc] (2016)
 - [7] S. A. Hojman, F. A. Asenjo, *Class. Quantum Grav.* **30**, 025008 (2013)
 - [8] C. Armaza, M. Banados, B. Koch, *Class. Quantum Grav.* **33**, 105014 (2016)
 - [9] C. W. Misner, K. S. Thorne, J. A. Wheeler, *Gravitation*, W. H Freeman & Company (1973)
 - [10] N. Straumann, *General Relativity with applications to Astrophysics*, Springer, Berlin (2009)
 - [11] R. T. Jantzen, P. Carini, D. Bini, *Annals Phys.* **215**, 1 (1992)
 - [12] C. Chakraborty, K. P. Modak, D. Bandyopadhyay, *ApJ* **790**, 2 (2014)
 - [13] D. Chatterjee, C. Chakraborty, D. Bandyopadhyay, *JCAP* **01** (2017) 062
 - [14] J. M. Bardeen, *Astrophys. J* **162**, 71 (1970)
 - [15] J. M. Bardeen, W. H. Press, S. A. Teukolsky, *ApJ* **178**, 347 (1972)
 - [16] E. G. Gimon, P. Horava, *Phys. Lett. B* **672**, 299 (2009)
 - [17] J. B. Hartle, *Gravity: An introduction to Einstein's General relativity*, Pearson (2009)
 - [18] K. Sakina, J. Chiba, *Phys. Rev. D* **19**, 2280 (1979)
 - [19] D. Malafarina, P. S. Joshi, arXiv:1603.02848v1 (2016)
 - [20] Z. Li, C. Bambi, *JCAP* **03** (2013) 031
 - [21] M. Patil, P.S. Joshi, *Class. Quantum Grav.* **28**, 235012 (2011)
 - [22] M. Patil, P.S. Joshi, *Phys. Rev. D* **84**, 104001 (2011)
 - [23] M. Banados, J. Silk, S. West, *Phys.Rev.Lett.* **103**, 111102 (2009)
 - [24] T. Harada and M. Kimura *Class. Quantum Grav.* **31** 243001 (2014)
 - [25] M. Patil, T. Harada, K. Nakao, P.S. Joshi, M. Kimura *Phys. Rev. D* **93**, 104015 (2016)
 - [26] J. Schnittman, *Phys. Rev. Lett.* **113** 261102, (2014)
 - [27] A. T. Okazaki, S. Kato, J. Fukue, *PASJ* **39**, 457 (1987)
 - [28] S. Kato, *PASJ* **42**, 99 (1990)
 - [29] J. Lense, H. Thirring, *Phys. Z.* **19**, 156-163, (1918)
 - [30] T. M. Belloni, L. Stella, *Space Sci Rev* **183**, 43, (2014)
 - [31] Z. Stuchlik, *Astronomical Institutes of Czechoslovakia, Bulletin* **31**, 129 (1980)
 - [32] D. Pugliese, H. Quevedo, R. Ruffini, *Phys. Rev. D* **84**, 044030 (2011)
 - [33] I. F. Ranea-Sandoval, H. Vucetich, *Relativity and Gravitation* **157**, 435 (2014)
 - [34] S. Chandrasekhar, *The Mathematical Theory of Black Holes*, Oxford (1992)
 - [35] T. M. Belloni, L. Stella, *Space Science Reviews* **183**, 43 (2014)
 - [36] T. Belloni, A. Sanna, M. Méndez, *MNRAS* **426**, 1701 (2012)
 - [37] L. Stella, M. Vietri, *ApJ* **492**, L59 (1998)
 - [38] L. Stella, M. Vietri, *Phys. Rev. Lett.* **82**, 17 (1999)

- [39] A. Ingram, S. Motta, *MNRAS* **444**, 2065 (2014)
- [40] S. Motta et al., *MNRAS* **437**, 2554 (2014) ; S. Motta et al., *MNRAS* **439**, L65 (2014)
- [41] L. Stella, A. Possenti, *Space Sci. Rev.* **148**, 105 (2009)
- [42] A. Ingram et. al, *MNRAS* **461**, 1967 (2016)
- [43] G. Török, Z. Stuchlik, *Astronomy and Astrophysics* **437**, 775 (2005)
- [44] Z. Stuchlik, J. Schee, *Class. Quantum Grav.* **29**, 065002 (2012)